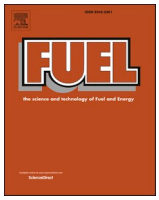
Fuel 307 (2022) 121803



Contents lists available at ScienceDirect

Fuel

journal homepage: www.elsevier.com/locate/fuel



Full Length Article



# Facile preparation of amorphous $Ce_nMnO_x$ catalysts and their good catalytic performance for soot combustion

Di Yu [a], Chao Peng [a], Xuehua Yu [a,*], Lanyi Wang [b], Kaixiang Li [c], Zhen Zhao [a,b,*], Zhenguo Li [c,*]

[a] Institute of Catalysis for Energy and Environment, College of Chemistry and Chemical Engineering, Shenyang Normal University, Shenyang 110034, China
[b] State Key Laboratory of Heavy Oil Processing, China University of Petroleum Beijing 102249, China
[c] National Engineering Laboratory for Mobile Source Emission Control Technology, China Automotive Technology & Research Center Co., Ltd., Tianjin 300300, China

ARTICLE INFO

*Keywords:*
Amorphous $Ce_nMnO_x$
Catalysts
Soot particles
Combustion

ABSTRACT

Diesel engines are widely used because of their low fuel consumption, high fuel efficiency, high reliability, and safety. However, the soot particles contained in diesel engine exhaust have become one of the main sources of urban haze, and their elimination has great significance for environmental protection and economics. In the present study, a series of $Ce_nMnO_x$ catalysts with different Ce contents and calcination temperatures were successfully synthetized via a simple hydrothermal process, and the physicochemical characteristics of the as-prepared catalysts were investigated. That $Ce_nMnO_x$ composite oxides were amorphous, contradicting previous reports that manganese and cerium usually form $Mn_xCe_{1-x}O_\delta$ with crystalline structures. Due to Ce doping, the amorphous $Ce_1MnO_x$ catalysts have higher specific surface area, greater porosity, and better ability to activate oxygen species than pure $MnO_x$ catalysts. The amorphous catalysts also exhibit good stability, sulfur and water resistance for catalytic combustion of soot particles. Among the prepared catalysts, $Ce_1MnO_x$ calcinated at 450 °C has the best catalytic activity, the values of $T_{10}$, $T_{50}$ and $T_{90}$ were 258 °C, 327 °C and 370 °C, respectively. Based on their simple preparation, low cost, and good catalytic performance, the amorphous $Ce_nMnO_x$ catalysts show promise for application in soot combustion.

## 1. Introduction

Diesel engines have been found an increasingly wide utilization in heavy vehicles and construction machinery. They are also increasingly employed in light vehicles and cars because of their advantages of high-power performance, high reliability, low fuel consumption and safety [1-4]. However, the pollutants emitted from diesel engines, which include carbon monoxide (CO), nitrogen oxide ($NO_x$), hydrocarbon, and soot particles, can cause serious harm to the environment. In particularly, soot particles are important source for haze and have been attracted extensive concern. Moreover, soot particles can absorb a variety of organic pollutants, heavy metals, and carcinogens, and they can be easily inhaled, causing a variety of diseases [5-7]. Therefore, it is urgent to reduce the emission of soot particles. At present, diesel post-treatment technology is one of the most economical and effective ways to remove soot. In this approach, soot particles are captured by a diesel particulate filter (DPF). However, the spontaneous combustion of soot particles occurs at 550 °C–600 °C, while the temperature of diesel engine exhaust outlet ranges from 150 °C to 450 °C. Thus, some current research focuses on eliminating trapped soot particles under the range of diesel engine exhaust temperatures. One of the most effective ways to accelerate soot elimination is to coat the DPF with catalysts and form a catalyzed DPF (CDPF). CDPF containing catalysts with high activity can promote soot burning and realize the passive regeneration of DPF. Therefore, the design and preparation of highly efficient catalysts has significant benefits for environmental protection and economics.

To date, noble metal catalysts [8-10], manganese-based catalysts [11,12], cerium-based catalysts [13-16], and perovskite oxide [17-20] have been designed and prepared for soot combustion. Among these catalysts, manganese-based oxides ($MnO_x$) have been recognized as a research hotspot in heterogeneous catalysis owing to low cost, high thermal stability and high oxidation–reduction ability resulting from the multiple valence states of Mn (+2, +3, and +4)[21,22]. Previous works have demonstrated that most metal ions (e.g., $Fe^{3+}$, $Co^{2+}$, $Cu^{2+}$, $V^{5+}$,

* Corresponding authors at: Institute of Catalysis for Energy and Environment, College of Chemistry and Chemical Engineering, Shenyang Normal University, Shenyang 110034, China (Xuehua Yu and Zhen Zhao); National Engineering Laboratory for Mobile Source Emission Control Technology, China Automotive Technology & Research Center Co., Ltd., Tianjin 300300, China (Zhenguo Li).
*E-mail addresses:* yuxuehua1986@163.com (X. Yu), zhenzhao@cup.edu.cn (Z. Zhao), lizhenguo@catarc.ac.cn (Z. Li).

https://doi.org/10.1016/j.fuel.2021.121803
Received 15 April 2021; Received in revised form 31 July 2021; Accepted 22 August 2021
Available online 2 September 2021
0016-2361/© 2021 Elsevier Ltd. All rights reserved.

and $Ni^{2+}$) can be well doped into $MnO_x$ because of its special layered structure (2 × ∞, 3 × ∞) and pore structure (2 × 2, 3 × 3, etc.). $MnO_x$ modified by different metal ions (M-$MnO_x$) exhibit excellent activity for $DeNO_x$, elimination of volatile organic compounds, and soot combustion [23-27]. Soot oxidation reaction, as we all know, is a gas–solid (catalyst)–solid (soot) three-phase deep oxidation process. To efficiently remove soot particles, it is essential to enhance the contact efficiency of the catalyst and soot particles, and possess high redox capacity and oxygen activation ability at low temperature. The ions introduced into the framework or pore structure of $MnO_x$ can modify the physicochemical properties of $MnO_x$. M−$MnO_x$ can be considered as potential catalysts for soot combustion owing to their special physicochemical properties [28-31]. Cerium (Ce), which has been known to act a pivotal part in catalysis for automobile exhaust purification, has been widespread applied in automotive three-way catalysts for a long time. Cerium oxide has a strong capacity for oxygen storage and release because the valence states of Ce can be converted between +3 and +4. When the oxygen content in the exhaust gas is sufficient, the form of cerium oxide changes from $Ce_2O_3$ to $CeO_2$ via the oxidation reaction $Ce_2O_3 + 1/2O_2 \rightarrow 2CeO_2$, thereby storing the oxygen from the exhaust gas. When the oxygen content is insufficient, the form of cerium oxide changes from $CeO_2$ to $Ce_2O_3$ via the reduction reaction $2CeO_2 \rightarrow Ce_2O_3 + 1/2O_2$. Based on the above reactions, cerium oxide can ameliorate the activity of a catalyst by facilitating the storage and release of oxygen [32-35].

The doping of Ce into $MnO_x$ is considered as an effective way to further promote the catalytic activities of $MnO_x$ catalysts. The variable valence state of Ce promotes the production of oxygen vacancies, which improves the ability to activate molecular oxygen. Meanwhile, the prominent oxygen storage and release capacity of Ce can further enhance the supply of oxygen species for soot combustion [36-39]. Herein, we develop a hydrothermal method for preparing cerium–manganese oxides($Ce_nMnO_x$) with different Ce contents and calcination temperatures. The characterization such as X-ray diffraction, $N_2$ physisorption, $H_2$ temperature-programmed reduction are measured to analyze the physicochemical characteristics of the manganese–cerium oxide catalysts. The activities and stabilities of the as-prepared catalysts for soot oxidation were also evaluated. The results demonstrate that amorphous $Ce_nMnO_x$ catalysts with different Ce contents and calcination temperatures were synthesized successfully by the hydrothermal method, with some exhibiting excellent performance for soot combustion. The results differ from the findings of past studies suggesting that Mn–Ce oxide complexes are generally formed with $CeO_2$ or $MnO_2$ crystalline structures [40-42].

## 2. Experimental

### 2.1. Synthesis of $Ce_nMnO_x$ catalysts

The $Ce_nMnO_x$ catalysts were synthetized via a hydrothermal process. Typically, 3.16 g $KMnO_4$ (99.5%, Sinopharm) was dissolved in 100 mL of deionized water, then, a certain amount of $Ce(NO_3)_3{\cdot}6H_2O$ (99.0%, Sinopharm) was added to 20 mL of 2 mol·$L^{-1}$ HCl (Sinopharm) solution to obtain a clarified solution. The above solutions were mixed and stirred for 30 min. Afterwards, the mixture was hydrothermally treated at 120 °C for 12 h in a stainless steel Teflon-lined autoclave, and then the autoclave was cooled. The products were filtered and washed for 3–5 times until the washed water became neutral (pH = 7). The precursor products were dried at 80 °C for 12 h, and calcined at 550 °C for 4 h by a heating rate of 5 °C/min. Finally, $Ce_nMnO_x$ catalysts were obtained after cooling at room temperature, where n is the Ce/Mn molar ratio of the precursor solution, and the values are 0, 0.2, 0.5, 1, 1.5 and 2, respectively. To study the impact of calcination temperature, a series of $Ce_1MnO_x$ catalysts were calcined at 450, 650, 750, 850, 950 °C respectively. To more clearly express the raw material composition and amount of $Ce_nMnO_x$ catalysts prepared with different Ce doping amounts and different calcination temperatures, the synthetic schemes of catalysts are shown in Table 1.

### 2.2. Synthesis of $Ce_1/MnO_x$ catalyst

For comparison, $Ce_1/MnO_x$ catalyst was synthetized by incipient-wetness impregnation method. Firstly, 1.49 g $Ce(NO_3)_3{\cdot}6H_2O$ was added to 2 mL of deionized water and formed solution in a beaker, and then the above solution was impregnated on 0.3 g synthesized $MnO_x$. The obtained precursor was dried at 80 °C and then calcined at 550 °C for 4 h by a heating rate of 5 °C/min. Finally, $Ce_1/MnO_x$ catalyst was obtained.

### 2.3. Characterizations

The phase structures of catalysts were measured by X-ray diffractometer (Ultima IV, Rigaku) with Cu Kα radiation. Data were recorded in the range of 10°-80° with an increment of 0.02°. The scanning speed was 5°/min.

The morphologies of catalysts were obtained on a field-emission scanning electron microscope (Hitachi S-4800, Japan). The SEM measurement parameter of the accelerating voltage were 200 V – 30 kV.

The visible Raman spectra (scanning range from 100 to 1000 $cm^{-1}$) and the UV Raman spectra (scanning range from 100 to 1600 $cm^{-1}$) were recorded on a spectrometer (HORIBA LabRAM HR Evolution) with a 532-nm and 325-nm lasers, respectively.

The textural properties of catalysts were characterized by $N_2$ physisorption at − 196 °C, with Micromeritics TriStar II:3020. Prior to analysis, the catalysts were degassed at 300 °C for 4 h.

The surface chemical compositions and chemical states of catalysts was characterized by X-ray photoelectron spectroscopy using a Thermo ESCALAB 250Xi instrument. The binding energy was calibrated with C1s = 284.8 eV.

$H_2$-TPR measurements were conducted on a chemical adsorption instrument (AutoChemi II2920). The catalysts (50 mg) were pre-treated under flowing $N_2$ atmosphere for 1 h at 300 °C followed by cooling to 40 °C. Subsequently, the temperature was ramped to 850 °C under $H_2$/$N_2$ (50 mL/min) at 10 °C/min. TCD was applied to record the consumption of hydrogen and the amounts of $H_2$ consumed were calibrated with CuO.

Soot-TPR was performed in Ar at flow rate of 50 mL/min and the outlet gases were tested by the gas chromatograph (Agilent 7890B). The detailed measurement processes are as follow. 0.1 g catalyst and 0.01 g soot under loose contact mode were pretreated at 300 °C for 30 min in Ar (50 mL/min) to remove impurities. The temperature was raised from 100 °C to 750 °C by heating rate of 2 °C/min.

**Table 1**
Recipes for the synthesis of catalysts with different dosages of Ce doping and calcination temperature.

| Catalysts | $KMnO_4$/g | HCl/ml | Ce $(NO_3)_3{\cdot}6H_2O$/g | $H_2O$/ml | calcination temperature /°C |
|---|---|---|---|---|---|
| $MnO_x$ | 3.16 | 20 | – | 100 | 550 |
| $Ce_{0.2}MnO_x$ | 3.16 | 20 | 1.73 | 100 | 550 |
| $Ce_{0.5}MnO_x$ | 3.16 | 20 | 4.34 | 100 | 550 |
| $Ce_1MnO_x$ | 3.16 | 20 | 8.68 | 100 | 550 |
| $Ce_{1.5}MnO_x$ | 3.16 | 20 | 13.02 | 100 | 550 |
| $Ce_2MnO_x$ | 3.16 | 20 | 17.36 | 100 | 550 |
| $Ce_1MnO_x$-$T_{450}$ | 3.16 | 20 | 8.68 | 100 | 450 |
| $Ce_1MnO_x$-$T_{650}$ | 3.16 | 20 | 8.68 | 100 | 650 |
| $Ce_1MnO_x$-$T_{750}$ | 3.16 | 20 | 8.68 | 100 | 750 |
| $Ce_1MnO_x$-$T_{850}$ | 3.16 | 20 | 8.68 | 100 | 850 |
| $Ce_1MnO_x$-$T_{950}$ | 3.16 | 20 | 8.68 | 100 | 950 |

$O_2$-TPD were conducted on a chemical adsorption instrument (TP-5076, Tianjin Xianquan). The catalysts (100 mg) were pre-treated in air at for 1 h 300 °C and subsequently cooled to 40 °C. Afterwards, the temperature was ramped to 850 °C under He (50 mL/min) at 10 °C/min. TCD was used to record the desorption of oxygen species.

NO oxidation experiment was measured by temperature programmed oxidation (TPO) through the NOx Analyzer nCLD 62. Before the NO-TPO tests, 100 mg of catalysts were pretreated at 200 °C for 30 min under Ar (100 mL/min) to remove impurities. The temperature range of TPO was 100 °C – 500 °C with 2 °C/min. The NO oxidation reaction was performed with a mixed gas (flow rate 50 mL/min) including 10% $O_2$, 0.1% NO and Ar balanced.

Adsorption and desorption rate of oxygen was measured by the isothermal reactions with and without oxygen in the reaction gases, respectively. In each experiment, 0.1 g catalyst and 0.01 g soot under loose contact mode were pretreated at 200 °C for 30 min in Ar (150 mL/min) to remove impurities. For aerobic isothermal reaction, the sample was heated to 250 °C at a heating rate of 10 °C/min in Ar and 0.2% NO atmosphere and kept at 250 °C until the $CO_2$ signal stabilization. After that, 10% $O_2$ was inlet and the $CO_2$ signal was recorded by gas chromatograph for 1 h. For anaerobic isothermal reaction, the sample was heated to 250 °C at a heating rate of 10 °C/min in 10%$O_2$, 0.2% NO and Ar and kept at 250 °C until the $CO_2$ signal stabilization. After that, 10% $O_2$ was removed and the $CO_2$ signal was recorded by gas chromatograph for 1 h.

### 2.4. Activity measurements

The activity tests were measured by TPO reaction under loose contact mode. The temperature range of TPO was 100 °C–600 °C with 2 °C/min. The model soot was Printex-U particulates from Degussa with ~ 25 nm diameter. In the TPO experiment, 0.1 g catalyst and 0.01 g soot were mixed with a spatula to obtain the loose contact mode, and then placed in a fixed-bed tubular quartz reactor (Φ = 8 mm) The oxidation reaction was performed with a mixed gas, including 0.2% NO, 10% $O_2$ and Ar (balanced) at a flow rate of 50 mL/min. The gas chromatograph (Agilent 7890B) was used to analyze the outlet gas compositions. The activities of $Ce_nMnO_x$ and $Ce_1/MnO_x$ catalysts are estimated by the temperature $T_{10}$, $T_{50}$ and $T_{90}$, which are corresponding to 10%, 50% and 90% conversion of soot particles. The $CO_2$ selectivity ($S_{CO2}$) calculated by $S_{CO2} = C_{CO2}/(C_{CO} + C_{CO2})$, where $C_{CO2}$ and $C_{CO}$ are the outlet gas concentrations of $CO_2$ and CO. $S^m_{CO2}$ is the $CO_2$ selectivity and corresponding to the temperature with the highest soot combustion rate ($T_m$).

## 3. Results and discussion

### 3.1. Physicochemical properties of as-prepared catalysts

#### 3.1.1. XRD results

Fig. 1A displays the XRD results of $Ce_1/MnO_x$ and $Ce_nMnO_x$ with different Ce contents. As seen in Fig. 1Aa, the $MnO_x$ catalyst without Ce contains two crystal phases. The main peaks at 12.8°, 18.1°, 28.8°, 37.5°, and 49.8° are corresponded to the (1 1 0), (2 0 0), (3 1 0), (2 1 1), and (4 1 1) lattice planes, respectively, indicating the existence of crystalline cryptomelane-type $MnO_2$ (marked by ★) [43]. The three diffraction peaks appearing at 23.1°, 32.9°, and 55.1° belong to the (2 1 1), (2 2 2), and (4 4 0) reflections of the $Mn_2O_3$ crystal phase (marked by ◇) [44]. The catalyst doped with a little Ce ($Ce_{0.2}MnO_x$) is amorphous, and the diffraction peaks of cryptomelane-type $MnO_2$ and $Mn_2O_3$ do not appear in its XRD pattern (Fig. 1Ab). As the ratio of Ce/Mn increased to 1, the characteristic diffractions peaks disappeared (as shown in Fig. 1Ac and Ad for $Ce_{0.5}MnO_x$ and $Ce_1MnO_x$, respectively). The results illustrate that doping of Ce is changed the crystal form of $MnO_x$ and became an amorphous manganese–cerium oxide due to the destruction of the ordered $MnO_x$ lattice. As the Ce doping content increased further, there are two weak diffraction peaks at 28.6° and 33.0° (Fig. 1Ae and Af), corresponding to the (1 1 1) and (2 0 0) crystal planes of $CeO_2$ (marked by ▽). This indicates that $CeO_2$, which formed via the crystallization of excess Ce, coexisted with amorphous cerium–manganese oxide, and the crystallinity became stronger with increasing of the cerium content [45]. The XRD patterns in Fig. 1Ag show that $Ce_1/MnO_x$ contained $CeO_2$ and $MnO_x$ crystal phases. The main diffractions peaks of this catalyst can be indexed to the $CeO_2$ fluorite structure, and the intensity of the $MnO_x$ diffraction peak is relatively weak. The XRD results show that the method used to introduce Ce into $MnO_x$ has a major impact on the crystallization phase. The introduction of Ce through the hydrothermal treatment can destroy the crystalline structure of $MnO_x$, resulting in amorphous manganese–cerium oxide ($Ce_nMnO_x$).

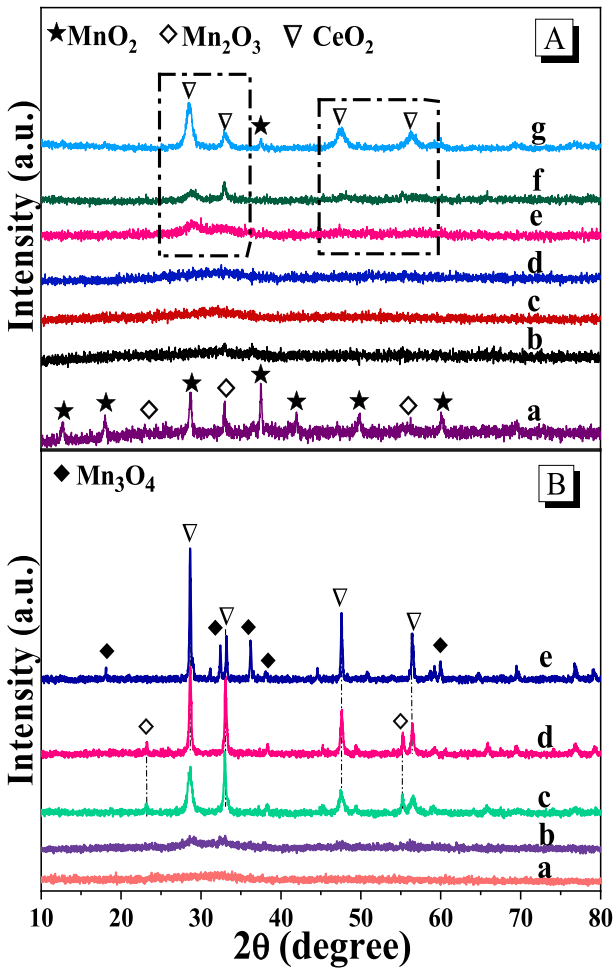



**Fig. 1.** XRD pattern of as-prepared catalysts (A: a: $MnO_x$; b: $Ce_{0.2}MnO_x$; c: $Ce_{0.5}MnO_x$; d: $Ce_1MnO_x$; e: $Ce_{1.5}MnO_x$; f: $Ce_2MnO_x$; g: $Ce_1/MnO_x$. B: a: $Ce_1MnO_x$-$T_{450}$; b: $Ce_1MnO_x$-$T_{650}$; c: $Ce_1MnO_x$-$T_{750}$; d: $Ce_1MnO_x$-$T_{850}$; e: $Ce_1MnO_x$ -$T_{950}$).

The effect of calcination temperature on the $Ce_1MnO_x$ samples were characterized by XRD. The XRD patterns of Fig. 1Ad, Ba, and Bb show that the $Ce_1MnO_x$ catalysts have none obvious diffraction peaks of manganese oxide or cerium oxide when the temperature was in the range from 450 °C to 650 °C. While the temperature was 750 °C or 850 °C, the characteristic diffraction peaks of $CeO_2$ (28.6°, 33.0°, 47.5°, and 56.3°) and $Mn_2O_3$ (23.1° and 55.1°) were observed (Fig. 1Bc and 1Bd). As the temperature increased further to 950 °C, the XRD pattern of $Ce_1MnO_x$-$T_{950}$ indicated a mixture of $CeO_2$ and $Mn_3O_4$ phases. The diffraction peaks at 18.0°, 32.3°, 36.1°, and 59.8° are belonged to (1 0 1), (1 0 3), (2 1 1) and (2 2 4) crystal planes of $Mn_3O_4$, respectively (marked by ◆ in Fig. 1Be) [46]. Based on the above XRD patterns, the calcination

temperature was one of the key factors on the crystal states and crystal phases of the $Ce_1MnO_x$ catalyst. A higher temperature caused the release of doped cerium ions, resulting in causing the amorphous $Ce_nMnO_x$ catalysts to be converted into mixed-phase oxides containing $CeO_2$, $Mn_2O_3$, $Mn_3O_4$, and so on.

### 3.1.2. SEM analysis

The morphologies of the $Ce_nMnO_x$ and $Ce_1/MnO_x$ catalysts were characterized by SEM (Fig. 2). As shown in Fig. 2A and B, the $MnO_x$ catalyst had a dendrite morphology resulting from the cross-stacking of nanorods with lengths of 0.3–3 μm and diameters of 50–200 nm. In contrast, the hydrothermally prepared $Ce_nMnO_x$ catalysts formed micron-scale clusters of agglomerated nanoparticles (Fig. 2C–H). The surfaces of the $Ce_nMnO_x$ catalysts were composed by nanoparticles with sizes of approximately 50–100 nm. The particle size and the degree of agglomeration increased slightly with the increase of Ce doping. From Fig. 2, it is obvious illustrated that the morphology of the $Ce_1/MnO_x$ catalyst is somewhat alike to that of $MnO_x$. However, the entire surface of $Ce_1/MnO_x$ was covered with a thick layer of $CeO_2$. This result is supported by the weak $MnO_x$ peaks in the XRD pattern of $Ce_1/MnO_x$ (Fig. 1Ag), which also suggest that the surface of $MnO_x$ was covered by $CeO_2$.

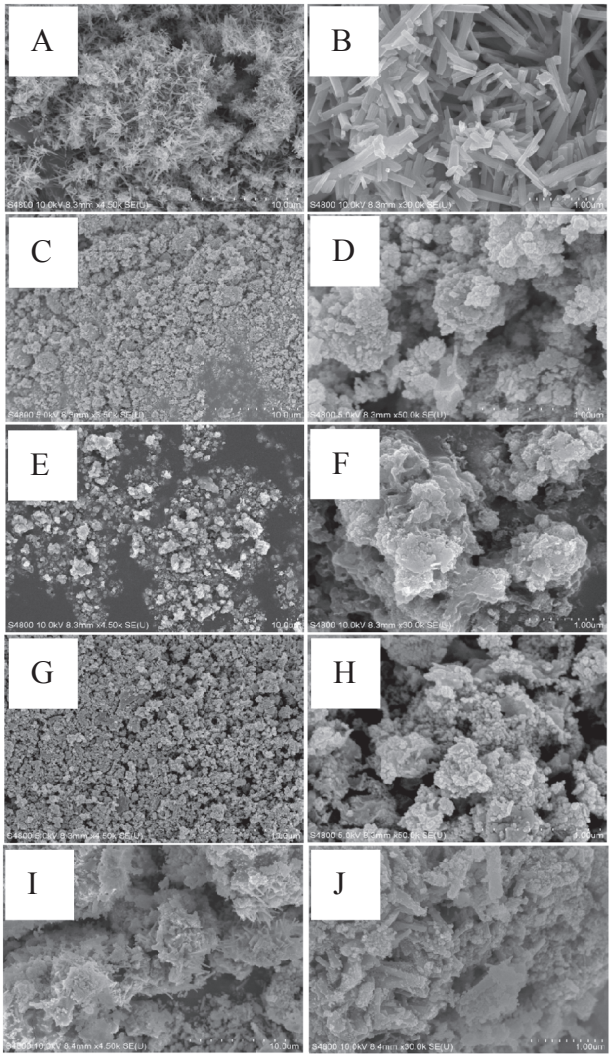



**Fig. 2.** SEM images of as-prepared catalysts (A, B: $MnO_x$; C, D: $Ce_{0.2}MnO_x$; E, F: $Ce_1MnO_x$; G, H: $Ce_2MnO_x$; I, J: $Ce_1/MnO_x$).

### 3.1.3. Raman spectroscopy analysis

The valence-bond structure of the catalysts was analyzed by the Raman spectra. For the $MnO_x$ and $Ce_1/MnO_x$ catalysts (Fig. 3a and 3e, respectively), the weak bands located at 181 $cm^{-1}$ correspond to the deformation modes of Mn–O–Mn. The peaks centered at 638 $cm^{-1}$ can be assigned to the stretching vibration of Mn–O, which was perpendicular to the direction of the $MnO_6$ basal octahedral chains. These peaks are indicative of a well-developed 2 × 2 tunnel structure [47,48]. The bands at 345 $cm^{-1}$ in the spectra of the $MnO_x$ correspond to the out-of-plane bending modes of $Mn_2O_3$ [49,50]. Compared to the $MnO_x$ catalyst, $Ce_nMnO_x$ gave rise to a much broader and weaker peak located at 638 $cm^{-1}$. This difference can be attributed to inhomogeneous strain broadening associated with particle size dispersion and phonon confinement, which was in agreement with the SEM results [51,52]. The disappearance of the peak at approximately 181 $cm^{-1}$ in the spectrum of $Ce_nMnO_x$ further indicates that doping with Ce distorted the Mn–O–Mn and Mn–O bond vibrations, resulting in the transformation of the tunnel structure of $MnO_x$. Moreover, the obvious vibration peaks at approximately 460 and 575 $cm^{-1}$ of the $Ce_1/MnO_x$ catalyst are characteristic of $CeO_2$. These bands correspond to the symmetrical stretching vibrations of oxygen atoms around $Ce^{4+}$ in cubic $CeO_2$ [53,54]. As the Ce/Mn ratio increased further to 2 in the hydrothermally formed $Ce_nMnO_x$ catalyst, the vibration peak of $CeO_2$ shifted obviously from 460 to 441 $cm^{-1}$. Meanwhile, the peak located at 575 $cm^{-1}$ disappeared when Ce was introduced into the $Ce_nMnO_x$ catalysts. The Raman results further confirm that the hydrothermal doping of Ce into $MnO_x$ resulted in fundamentally different valence bond structure and surface properties compared to $Ce_1/MnO_x$ obtained using incipient wetness impregnation.

### 3.1.4. $N_2$ Physisorption analysis

The $N_2$ adsorption and desorption isotherms of the $Ce_nMnO_x$ and $Ce_1/MnO_x$ were displayed in the Fig. 4. The catalysts exhibited type Ⅳ isotherms and H3 hysteresis loops. The adsorption volume of $N_2$ increased rapidly at $P/P_0$ = 0.7–1.0, demonstrating that the catalysts had irregular pore structures resulting from the accumulation of particles. The pore size distribution curves in Fig. 4 demonstrate that the synthetic method used to introduce cerium ions obviously affected the pore structure of the catalyst. The $MnO_x$ catalyst had only a few accumulated mesopores with diameters of 2–4 nm (Fig. 4A). As shown in Fig. 4B, C, and D, the accumulated mesopores of $Ce_{0.2}MnO_x$, $Ce_1MnO_x$, and $Ce_2MnO_x$ had diameters of 5–15, 5–45, and 5–30 nm, respectively. The pore volume gradually increased with increasing Ce content. In

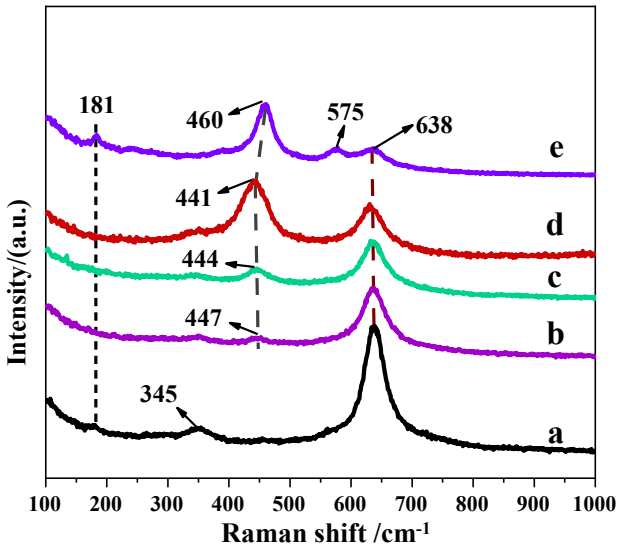



**Fig. 3.** Raman spectra of as-prepared catalysts (a: $MnO_x$; b: $Ce_{0.2}MnO_x$; c: $Ce_1MnO_x$; d: $Ce_2MnO_x$; e: $Ce_1/MnO_x$).

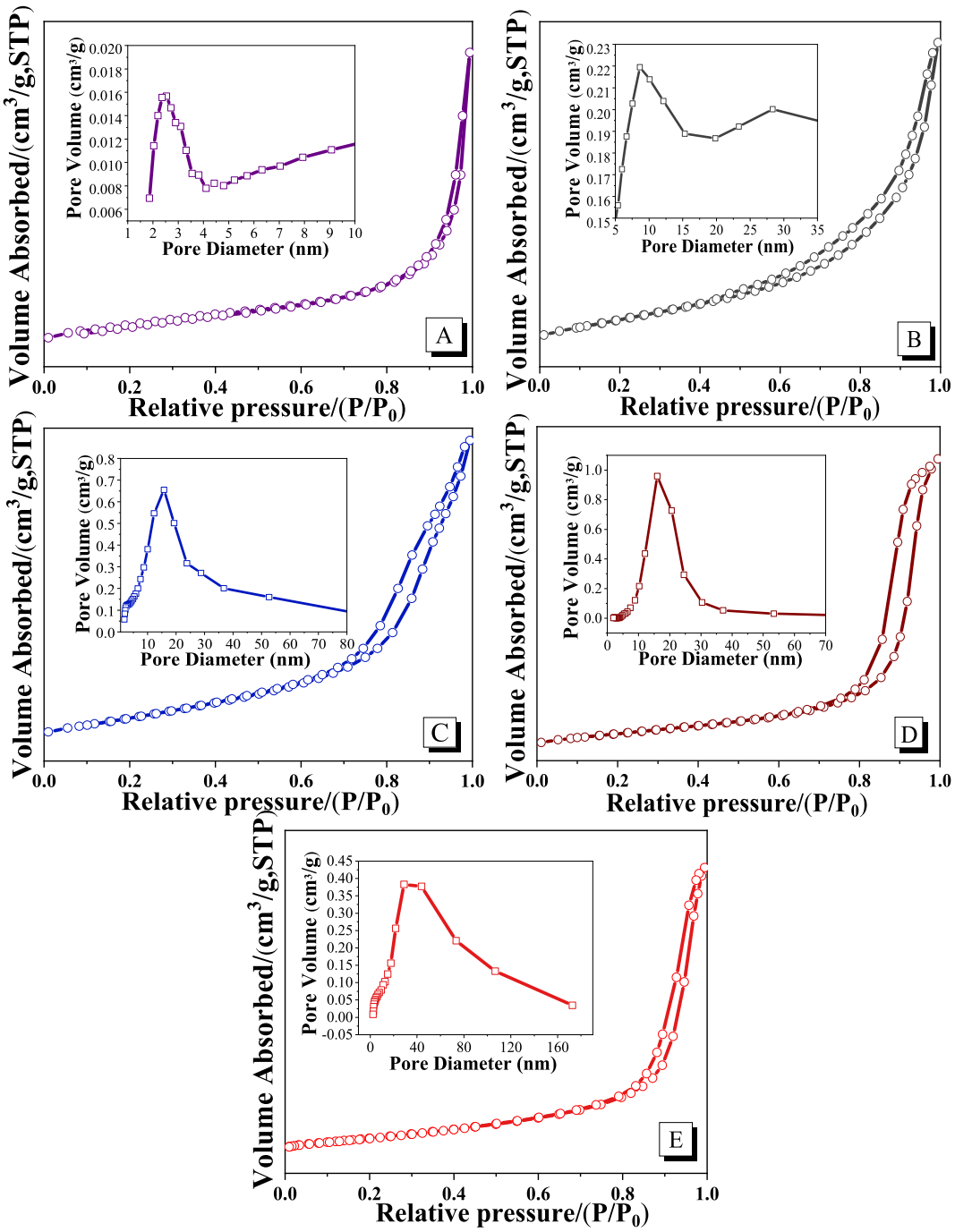



**Fig. 4.** $N_2$ adsorption desorption isothermal curve and pore diameter distribution curves of as-prepared catalysts (A: $MnO_x$; B: $Ce_{0.2}MnO_x$; C: $Ce_1MnO_x$; D: $Ce_2MnO_x$; E: $Ce_1/MnO_x$).

contrast, the $Ce_1/MnO_x$ catalyst prepared via incipient wetness impregnation had a mesoporous–macroporous structure with pore diameters of 20–140 nm (Fig. 4E). The pore structure of $Ce_1/MnO_x$ was primarily derived from the accumulation of $CeO_2$ covering the surface and rod-like $MnO_x$.

The textural properties of the $Ce_nMnO_x$ and $Ce_1/MnO_x$ catalysts are shown in Table 2. For $MnO_x$, the specific surface area and pore volume are 12.7 $m^2/g$ and 0.04 $cm^3/g$. However, the specific surface area of the catalyst increased significantly upon Ce ion doping into $MnO_x$. The specific surface area and pore volume of the $Ce_{0.2}MnO_x$ catalyst were 113.9 $m^2/g$ and 0.34 $cm^3/g$, while those of $Ce_1MnO_x$ were 150.7 $m^2/g$ and 0.48 $cm^3/g$. Considering XRD and SEM results, the obvious enhancements of the surface area and pore volume with increasing Ce content may be related to the inhibition of the formation of $MnO_x$ rod-like structures and the directional growth of crystalline $MnO_x$. Consequently, we can conclude that the surface area and pore volume formed by accumulated pores were greatly increased by nanosized $Ce_nMnO_x$ particles. However, when the Ce/Mn ratio increased from 1 to 2, the specific surface area was sharply decreased to 64.8 $m^2/g$. Based on the XRD and SEM results, this phenomenon can be explained as follows. Excessive Ce could not be effectively doped into the $MnO_x$ lattice and instead formed $CeO_2$ particles on the catalyst surface. These particles accumulated in the pore channels of the accumulated pores, thereby reducing the surface area of the catalysts. Meanwhile, numerous $CeO_2$ particles agglomerated on the catalyst surface, which further reduced the specific surface area and pore volume. Furthermore, as shown in

**Table 2**
Textural properties of as-prepared catalysts.

| Catalysts | Surface area ($m^2$/g)[a] | Total pore volume ($cm^3$/g)[b] | Pore size (nm)[c] |
|---|---|---|---|
| $MnO_x$ | 12.7 | 0.04 | 13.9 |
| $Ce_{0.2}MnO_x$ | 113.9 | 0.34 | 10.4 |
| $Ce_1MnO_x$ | 150.7 | 0.48 | 10.8 |
| $Ce_2MnO_x$ | 64.8 | 0.32 | 17.4 |
| $Ce_1/MnO_x$ | 48.6 | 0.31 | 19.5 |

a: Calculated by BET method; b: Calculated by BJH desorption cumulative volume of pores between 1.7 nm and 300 nm diameter; c: Calculated by BJH desorption average pore diameter; d: The crystallite sizes were estimated using XRD peak halfwidths by Scherrer equation.

Table 2, the specific surface area and pore volume of $Ce_1/MnO_x$ were 48.6 $m^2$/g and 0.31 $cm^3$/g, respectively, obviously larger than those of $MnO_x$ but smaller than those of $Ce_1MnO_x$. This is primarily because the $Ce_1/MnO_x$ catalyst consisted of a layer of $CeO_2$ particles on the surface of the $MnO_x$ support; that is, the morphology of the $Ce_1/MnO_x$ catalyst was not essentially different from that of $MnO_x$.

### 3.1.5. XPS analysis

The elemental composition, content, and valence state on the catalyst surface have important effects for soot combustion. To study the surface chemical states of Mn, Ce, and O, XPS measurements were performed over the $MnO_x$, $Ce_{0.2}MnO_x$, $Ce_1MnO_x$, and $Ce_2MnO_x$ catalysts. In the Ce 3d spectra (Fig. 5A), the Ce $3d_{3/2}$ and Ce $3d_{5/2}$ are in the range of 900–916 and 882–898 eV, respectively. The spectra can be fitted by eight peaks based on four pairs of spin–orbit doublets that correspond to Cerium ions with +3 and +4 valence states on the catalyst surface [55-57]. To maintain the charge balance, oxygen vacancies will be formed due to the appearance of $Ce^{3+}$, and the oxygen vacancy content increases with increasing $Ce^{3+}$ content. As shown in Table 3, among the catalysts, $Ce_1MnO_x$ had the highest $Ce^{3+}$ content of 23.7%, indicating that $Ce_1MnO_x$ possessed the most oxygen vacancies on its surface. These oxygen vacancies make it easier to adsorb oxygen and produce active oxygen species, which plays a major part for soot combustion.

In the Mn 2p spectra (Fig. 5B), the peaks of Mn are observed at 642.2 and 653.8 eV, which belong to Mn $2p_{3/2}$ and Mn $2p_{1/2}$. It is hard to accurately distinguish the valence states of Mn based on the Mn 2p binding energies because of the similar binding energies of $Mn^{2+}$, $Mn^{3+}$, and $Mn^{4+}$. Thus, the Mn 3s XPS spectra were also measured. According to the distinction of the Mn 3s multiplet splitting energy ($\Delta E$), the average oxidation state (AOS) can be calculated by AOS = 8.95–1.13$\Delta E$, allowing the different valence states and Mn contents in the catalysts to be determined [58-61]. According to the $\Delta E$ values in Fig. 5C, the calculated AOSs of the samples are displayed in Table 3. Based on the

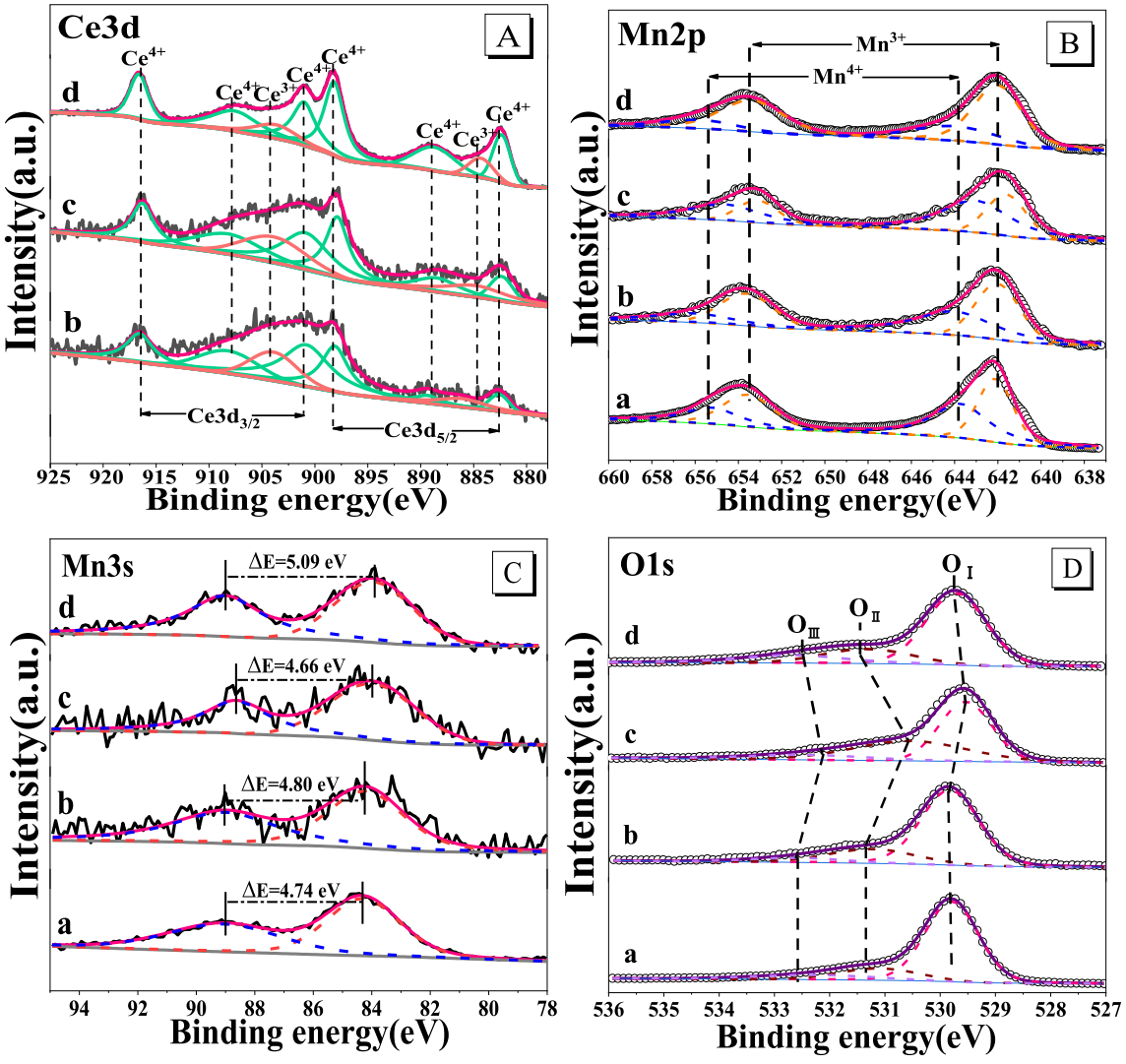



**Fig. 5.** XPS spectra of as-prepared catalysts (a: $MnO_x$; b: $Ce_{0.2}MnO_x$; c: $Ce_1MnO_x$; d: $Ce_2MnO_x$).

**Table 3**
Average oxidation states (AOS) and surface composition and oxidation states of Ce, Mn, O elements of as-prepared catalysts.

| Catalysts | AOS | R% | | R% | | R% | | |
|---|---|---|---|---|---|---|---|---|
| | | $Ce^{3+}$ | $Ce^{4+}$ | $Mn^{3+}$ | $Mn^{4+}$ | $O_I$ | $O_{II}$ | $O_{III}$ |
| $MnO_x$ | 3.59 | – | – | 51.6 | 48.4 | 74.7 | 15.7 | 9.6 |
| $Ce_{0.2}MnO_x$ | 3.53 | 19.4 | 80.6 | 52.7 | 47.3 | 72.9 | 20.5 | 6.6 |
| $Ce_1MnO_x$ | 3.68 | 23.7 | 76.3 | 35.9 | 64.1 | 49.9 | 38.3 | 11.8 |
| $Ce_2MnO_x$ | 3.20 | 13.2 | 86.8 | 75.0 | 25.0 | 66.6 | 18.8 | 14.6 |

AOS values, the oxidation states of Mn in the catalyst were determined to be +3 and +4 after fitting the peaks of Mn 2p. Among all the catalysts, the highest $Mn^{4+}$ content of ~64.1% was observed in $Ce_1MnO_x$. By contrast, the $Mn^{4+}$ content of the $Ce_2MnO_x$ catalyst was only 25%.

The O 1s peak of Fig. 5D fitting revealed three types of oxygen species on the prepared catalysts surface: $O_I$, $O_{II}$, and $O_{III}$, which correspond to lattice oxygen ($O^{2-}$), chemically adsorbed oxygen ($O_2^-$ and $O^-$) and physically adsorbed oxygen ($O_2$), respectively [62-64]. As shown in Table 3, the content of $O_{II}$ increased at first, and then decreased with increasing Ce content. Among the catalysts, $Ce_1MnO_x$ had the highest content of chemically adsorbed oxygen. The above analyzes indicate that the presence of $Ce^{3+}$, $Mn^{4+}$, and chemically adsorbed oxygen, which accelerates the production of oxygen vacancies, improved the activity for soot combustion.

### 3.1.6. $H_2$-TPR and $O_2$-TPD analyses

The redox properties of a catalyst have important effects for soot oxidation [65,66]. Therefore, the $Ce_nMnO_x$ catalysts were measured by $H_2$-TPR and $O_2$-TPD (Fig. 6A and 6B, respectively). Table 4 showed the $H_2$ consumption amounts of the catalysts. The reduction of manganese oxides under hydrogen atmosphere is generally considered by the following processes: $MnO_2 \rightarrow Mn_2O_3 \rightarrow Mn_3O_4 \rightarrow MnO$. From the Fig. 6Aa and Table 4, the reduction profiles of $MnO_x$ were decomposed into four components at 232 °C, 276 °C, 304 °C, and 322 °C, assigning to the surface chemically adsorbed oxygen, $MnO_2 \rightarrow Mn_2O_3$, $Mn_2O_3 \rightarrow Mn_3O_4$, and $Mn_3O_4 \rightarrow MnO$, respectively. As shown in Fig. 6Ab–6Ad, the $H_2$-TPR curves of the $Ce_nMnO_x$ catalysts could be split into four reduction peaks. Based on the XRD and XPS results, reduction peaks I, II, III, and IV correspond to the processes of surface physically adsorbed oxygen, chemically adsorbed oxygen, $Mn^{4+} \rightarrow Mn^3$ and $Mn^{3+} \rightarrow Mn^{2+}$, respectively [40,67,68]. Compared to the $MnO_x$ catalyst, reduction peaks I and II of $Ce_{0.2}MnO_x$ and $Ce_1MnO_x$ have lower reduction temperatures, while the reduction temperatures of $Ce_2MnO_x$ are higher. Among the catalysts, the lowest reduction temperatures were observed for $Ce_1MnO_x$ (194 °C, 232 °C, 262 °C, and 315 °C for peaks I, II, III, and IV, respectively). This demonstrates that hydrothermal doping with an appropriate amount of Ce can greatly reduce the reduction temperature of the catalyst. Compared to $Ce_1MnO_x$, the reduction temperatures of the $Ce_1/MnO_x$ catalyst were shifted toward higher temperature. In addition, as shown in Table 4, hydrogen consumption gradually decreased as the Ce content increased, while the hydrogen consumption of surface-adsorbed oxygen (peak I) first increased and then decreased. Among the catalysts, $Ce_1MnO_x$ had the highest hydrogen consumption of surface-adsorbed oxygen (0.458 mmol/g). The above results demonstrate that doping $MnO_x$ with an appropriate amount of Ce can enhance the fluidity of oxygen and promote oxygen migration in the catalyst to replenish surface oxygen species, thereby improving the catalytic performance [69,70].

According to the Fig. 6B of the $O_2$-TPD profiles, the desorption peaks of three oxygen species appear at 50 °C–200 °C, 250 °C–400 °C and

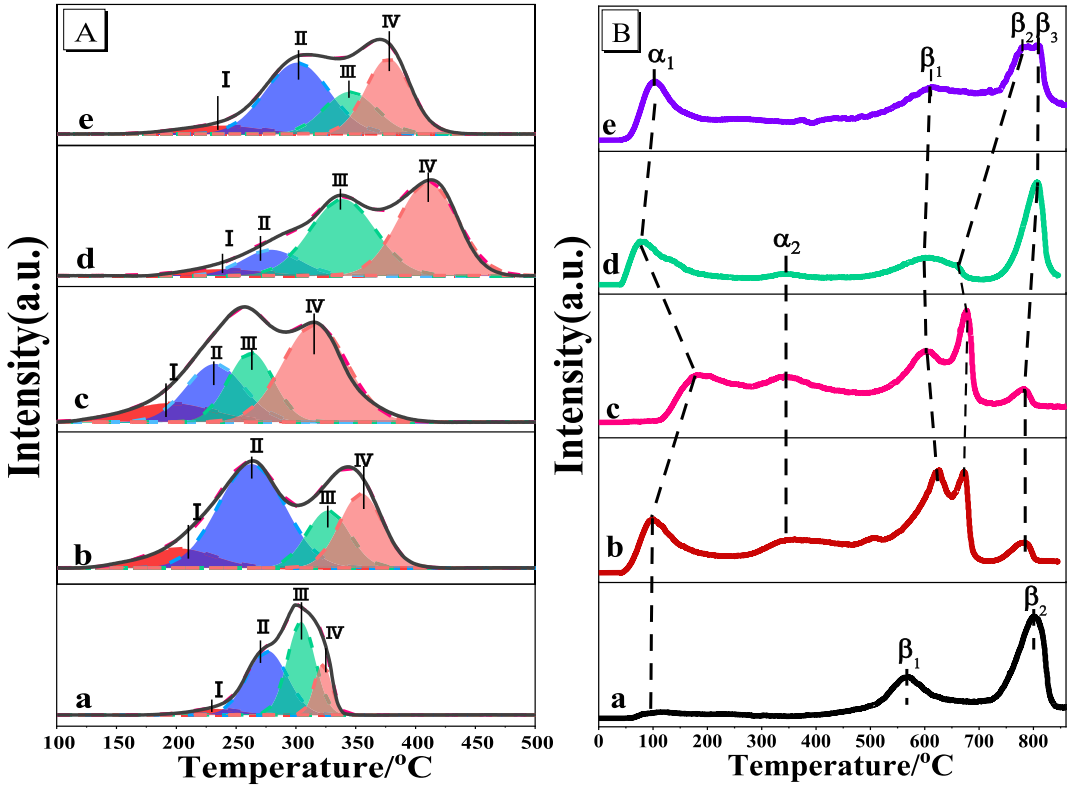



**Fig. 6.** $H_2$-TPR peak-fitting curves (A) and $O_2$-TPD curves (B) of as-prepared catalysts (a: $MnO_x$; b: $Ce_{0.2}MnO_x$; c: $Ce_1MnO_x$; d: $Ce_2MnO_x$; e: $Ce_1/MnO_x$).

**Table 4**
Peak temperature of $H_2$-TPR and hydrogen consumption of $H_2$ for as-prepared catalysts.

| Catalysts | Peak I | | Peak II | | Peak III | | Peak Ⅳ | | $H_2$ Consumption (mmol/g) |
|---|---|---|---|---|---|---|---|---|---|
| | T/°C | HC | T/ °C | HC | T/°C | HC | T/ °C | HC | |
| $MnO_x$ | 232 | 0.365 | 276 | 3.096 | 304 | 3.063 | 322 | 1.046 | 7.570 |
| $Ce_{0.2}MnO_x$ | 196 | 0.376 | 262 | 2.591 | 323 | 0.552 | 351 | 1.366 | 4.885 |
| $Ce_1MnO_x$ | 194 | 0.458 | 232 | 0.942 | 262 | 0.891 | 315 | 1.771 | 4.062 |
| $Ce_2MnO_x$ | 238 | 0.135 | 279 | 0.375 | 339 | 1.263 | 410 | 1.408 | 3.181 |
| $Ce_1/MnO_x$ | 237 | 0.157 | 301 | 1.077 | 345 | 0.520 | 377 | 0.801 | 2.555 |

500 °C–850 °C, which are corresponded to the desorption of surface or physically adsorbed oxygen ($O_2$ or $O_2^-{}_{surf}$, labeled as $\alpha_1$), chemically adsorbed oxygen ($O_2^-$ or $O^-$, labeled as $\alpha_2$), and lattice oxygen or oxygen in metal–oxygen bonds ($O^{2-}$, labeled as β), respectively [71-73]. The $\alpha_1$ peak of $Ce_1MnO_x$ was greater in intensity and appeared at higher temperature compared to the $\alpha_1$ peak of $MnO_x$. This difference may be associated with the production of more oxygen vacancies and the enhanced adsorption between $\alpha_1$ oxygen species and the catalyst surface for $Ce_1MnO_x$ compared to $MnO_x$.

Doping with Ce destroyed the crystalline structure of $MnO_x$, resulting in an amorphous phase. Compared to the crystalline catalysts, the amorphous catalysts contained more disordered metal–oxygen bonds, which are conducive to the generation of cations and defects on the surface of catalysts. Therefore, it had difficulty observing the $\alpha_2$ oxygen desorption peak in the $MnO_x$ and $Ce_1/MnO_x$ catalysts. The β oxygen desorption peak can be further divided into $\beta_1$, $\beta_2$, and $\beta_3$ in the range of 500 °C–850 °C. As shown in Fig. 6Bb–6Bd, $\beta_3$ peaks were observed for $Ce_{0.2}MnO_x$, $Ce_1MnO_x$, $Ce_2MnO_x$, and $Ce_1/MnO_x$, and the peak intensity increased with increasing Ce content. The XRD results show that crystalline $CeO_2$ gradually formed as the Ce content increased. Thus, the $\beta_3$ peak can be attributed to the desorption of Ce–O bands coincided with XRD results. For $MnO_x$ catalyst, the oxygen desorption peaks labeled $\beta_1$ and $\beta_2$ correspond to oxygen desorption in manganese oxide. Interestingly, although the temperatures of the other desorption peaks of the $Ce_nMnO_x$ catalysts were shifted toward higher temperature compared to those of $MnO_x$, the temperatures of the $\beta_2$ peaks were shifted to lower temperature. This is because Ce doping led to a transition from mixed crystalline phases to amorphous oxides, leading to changes in the oxygen desorption properties of manganese oxide.

### 3.2. Catalytic performance of as-prepared catalysts

#### 3.2.1. Activities test of the catalysts

The activities of catalysts are displayed in Table 5. In addition, the combustion of pure soot was also evaluated, its $T_{10}$, $T_{50}$, and $T_{90}$ values were 429 °C, 546 °C and 607 °C, respectively. In comparison, the $T_{10}$, $T_{50}$, and $T_{90}$ values were much lower when the catalysts were mixed with soot particles and evaluated under the loose contact mode, and the $CO_2$ selectivity was increased. This makes it clear that the as-prepared catalysts exhibit better activity for soot oxidation. From the Table 5, the performance of the $Ce_nMnO_x$ catalysts first increased and then decreased with increasing Ce content. Among the catalysts, $Ce_1MnO_x$ had the highest activity, its $T_{10}$, $T_{50}$, and $T_{90}$ and $CO_2$ selectivity were 268 °C, 332 °C, 369 °C and 99.4%, respectively. Furthermore, the calcination temperature exhibited a strong impact on catalytic performance. As the temperature increased, the activities of the catalysts decreased. When the calcination temperature was 450 °C, the $T_{10}$, $T_{50}$, and $T_{90}$ values of the $Ce_1MnO_x$ were 258 °C, 327 °C and 370 °C, respectively. With the calcination temperature increased to 950 °C, the $T_{10}$, $T_{50}$, and $T_{90}$ values of $Ce_1MnO_x$ were 331 °C, 401 °C and 449 °C, respectively. It is noticeable that the amorphous $Ce_1MnO_x$ catalyst exhibited better catalytic activity than $Ce_1/MnO_x$. Based on the physicochemical characteristics of the catalysts, the high activities of amorphous $Ce_nMnO_x$ catalysts are primarily attributed to the following two aspects. First, doping with Ce changed the morphology and structure of the catalyst (SEM results), resulting in the formation of numerous nanoparticles on the $Ce_nMnO_x$ catalyst surface along with a large quantity of accumulated pores in the interior of the catalyst (BET results). The modifications not only enhanced the effective contact of soot and the catalysts, they also facilitated the diffusion of micromolecular gases in the accumulated mesopores. In this way, the soot and reaction gases made full contact with the active sites of the $Ce_nMnO_x$ catalyst, which improved the utilization of active sites. Meanwhile, through nanoscale effects, the nanoparticles on the catalyst surface helped activate soot particles and micromolecular gases, further improving the catalytic performance. Second, according to $H_2$-TPR, $O_2$-TPD and XPS results, doping with an appropriate amount of Ce enhanced the amounts of $Ce^{3+}$, $Mn^{4+}$, and oxygen adsorbed on the catalyst surface. These changes in physicochemical properties were beneficial to the activation and generation of oxygen species, which are advantageous for catalytic performance.

**Table 5**
Catalytic activities of as-prepared catalysts for soot combustion.

| Catalysts | $T_{10}$/ °C | $T_{50}$/°C | $T_{90}$/ °C | $Sco_2^m$/% |
|---|---|---|---|---|
| Pure soot | 429 | 546 | 607 | 52.4 |
| $MnO_x$ | 300 | 367 | 405 | 99.1 |
| $Ce_{0.2}MnO_x$ | 272 | 347 | 391 | 99.1 |
| $Ce_{0.5}MnO_x$ | 273 | 339 | 379 | 99.4 |
| $Ce_1MnO_x$ | 268 | 332 | 369 | 99.4 |
| $Ce_{1.5}MnO_x$ | 265 | 336 | 379 | 98.9 |
| $Ce_2MnO_x$ | 286 | 360 | 404 | 98.8 |
| $Ce_1MnO_x$-$T_{450}$ | 258 | 327 | 370 | 99.6 |
| $Ce_1MnO_x$-$T_{650}$ | 284 | 349 | 390 | 99.6 |
| $Ce_1MnO_x$-$T_{750}$ | 299 | 356 | 395 | 99.5 |
| $Ce_1MnO_x$-$T_{850}$ | 302 | 364 | 405 | 98.9 |
| $Ce_1MnO_x$-$T_{950}$ | 331 | 401 | 449 | 94.8 |
| $Ce_1/MnO_x$ | 288 | 360 | 398 | 99.0 |

#### 3.2.2. Stability, sulfur and water resistance test of as-prepared catalysts

Catalyst stability is an important index for practical applications. The stability of the $Ce_1MnO_x$ catalyst was estimated by recycling the catalyst under the same conditions of experiments. Fig. 7A shows the results for the $Ce_1MnO_x$ catalyst during five reuses. The $T_{10}$, $T_{50}$, and $T_{90}$ of the $Ce_1MnO_x$ were 270 ± 3 °C, 335 ± 4 °C and 375 ± 6 °C, and the $CO_2$ selectivity exceeded 99%. This indicates that the $Ce_1MnO_x$ catalyst had high stability for soot oxidation. To verify whether the crystal phase of $Ce_1MnO_x$ changed after repeated reaction, XRD and Raman characterization was also carried out (Fig. 7Cb and 7Db). No obvious changes in the XRD pattern and Raman peak were observed after the catalyst was reused five times; thus, the crystal structure of the catalyst remained stable.

To further study the water and sulfur resistance of $MnO_x$, $Ce_1MnO_x$ and $Ce_1/MnO_x$ catalysts, the catalytic performances of catalysts were measured under varying conditions (Figs. 7B, 8A and B). For comparison, the $T_{10}$, $T_{50}$, and $T_{90}$ values of $MnO_x$, $Ce_1MnO_x$ and $Ce_1/MnO_x$ catalysts without water and $SO_2$ in the reaction gas were also presented. It can be clearly observed that $Ce_1MnO_x$ has higher water resistance and sulfur resistance than those of $MnO_x$ and $Ce_1/MnO_x$ catalysts. Evidently, the activity of $Ce_1MnO_x$ well maintained in the presence of 10% $H_2O$. However, the catalytic performances of catalysts were slightly lower

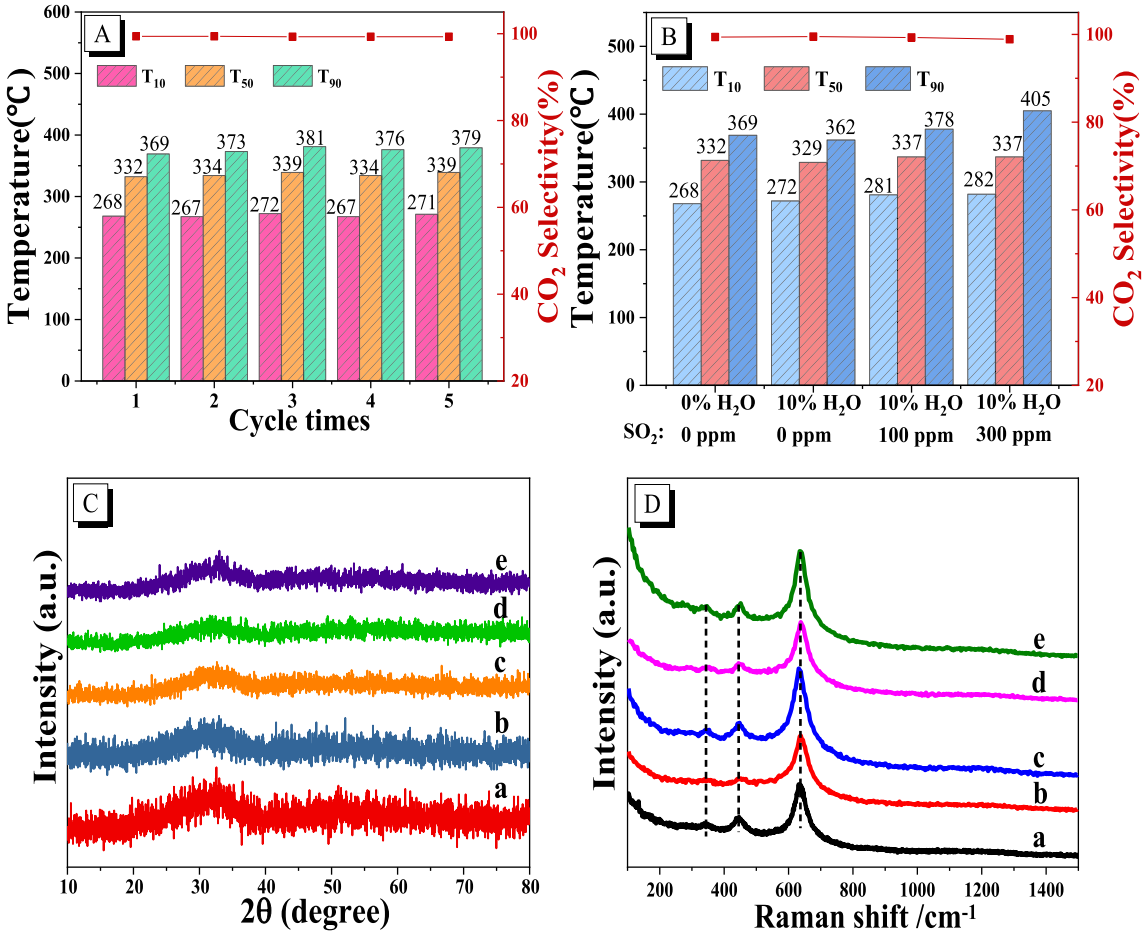



**Fig. 7.** The stability (A), tolerance of sulfur dioxide and water (B) and X-ray diffraction patterns (C) and Raman spectra (D) of used $Ce_1MnO_x$ under different treatment conditions (a: fresh $Ce_1MnO_x$; b: used $Ce_1MnO_x$ catalyst after 5 times; c: 10% $H_2O$ + 0 ppm$SO_2$; d: 10% $H_2O$ + 100 ppm$SO_2$; e: 10% $H_2O$ + 300 ppm$SO_2$).

when the reaction system consisted of 10%$H_2O$ and 100 ppm $SO_2$, the $T_{10}$, $T_{50}$, and $T_{90}$ values were 281, 337 and 378 °C, respectively. As the concentration of $SO_2$ increased to 300 ppm, the $T_{10}$ and $T_{50}$ values remained constant, while $T_{90}$ values increased to 405 °C. This indicated that the $SO_2$ affects the catalytic performance of catalysts to an extent. Furthermore, the value of $CO_2$ selectivity keeps higher than 98% under different reaction conditions. For the $MnO_x$ and $Ce_1/MnO_x$ catalysts, the $T_{10}$, $T_{50}$, and $T_{90}$ values increased significantly with the concentration of $SO_2$ increased to 300 ppm, and the $CO_2$ selectivity decreased to 93%. To more deeply verify the properties of catalysts, the XRD and Raman spectroscopy characterization of the catalysts after reaction were carried out. As evidenced by the results (Figs. 7Cc-e, Dc-e, 8Ca-d and Da-d), there were no significant differences in the phase and valence bond structure among the samples under different reaction conditions, which indicating that $SO_2$ did not enter bulk phase of catalysts to form sulfate. These results demonstrated that $Ce_1MnO_x$ catalyst has high water and sulfur resistance.

### 3.2.3. *NO-TPO tests of as-prepared catalysts*

As one of main components, $NO_x$ is an inevitable gas in the exhausts of diesel engines. It was patently obvious that the $NO_x$ is an essential factor for soot combustion. Thus, the $NO_2$ concentration (Fig. 9A) and NO concentration profile (Fig. 9B) during NO oxidation over $MnO_x$, $Ce_1/MnO_x$ and $Ce_1MnO_x$ catalysts were tested. It can be easily seen from Fig. 9A that the $NO_2$ concentration of $MnO_x$ and $Ce_1/MnO_x$ catalysts increased significantly at first and then decreased in the temperature range of 100–500 °C. The corresponding temperature of maximum $NO_2$ concentration is about 310 °C. In contrast to $MnO_x$ and $Ce_1/MnO_x$, a larger content of $NO_2$ can be generated with the assistance of $Ce_1MnO_x$ catalyst and the corresponding temperature of maximum $NO_2$ concentration is evidently reduced to 246 °C. It can be seen from the above comparison that $Ce_1MnO_x$ can rapidly convert NO to $NO_2$ at low temperature, indicating that $Ce_1MnO_x$ possessed better catalytic ability for NO oxidation. From the Fig. 9 (B), the trend of NO concentration of $MnO_x$, $Ce_1/MnO_x$ and $Ce_1MnO_x$ catalysts is completely opposite to that of $NO_2$ concentration, which further verifies the catalytic role during the NO oxidation reaction. Moreover, NO is catalytically oxidized almost entirely to $NO_2$ with the presence of $Ce_1MnO_x$ in favor of the catalytic oxidation of soot. The conclusion can be drawn that the soot is mainly oxidized by $NO_2$ converted from NO, rather than directly oxidized by $O_2$ during the soot oxidation. As a result, relatively high activity of $Ce_1MnO_x$ catalyst was obtained for soot combustion because of the excellent NO oxidation ability.

### 3.2.4. *Possible reaction mechanism of $Ce_1MnO_x$ and $Ce_1/MnO_x$ catalysts*

To further study the intrinsic activity of $Ce_1MnO_x$ and $Ce_1/MnO_x$ catalysts, the isothermal reaction with $O_2$ at 523 K (250 °C) was carried out and the reaction rate, active oxygen (O*) content and TOF value were calculated. It was obvious from Table 6 that the $Ce_1MnO_x$ exhibits higher reaction rate than $Ce_1/MnO_x$, and the reaction rate of $Ce_1MnO_x$ is about 2.5 times as much as that of $Ce_1/MnO_x$. The results illustrate that the active sites of $Ce_1MnO_x$ possessed better catalytic efficiency in the TPO reactions. On the other side, the amount of active oxygen (O*) of $Ce_1MnO_x$ is about 1.9 times that of $Ce_1/MnO_x$, which was a vital component in promoting the soot combustion process. From the Table 6, TOF value for $Ce_1/MnO_x$ (0.67) was lower than that of $Ce_1MnO_x$ (0.89),

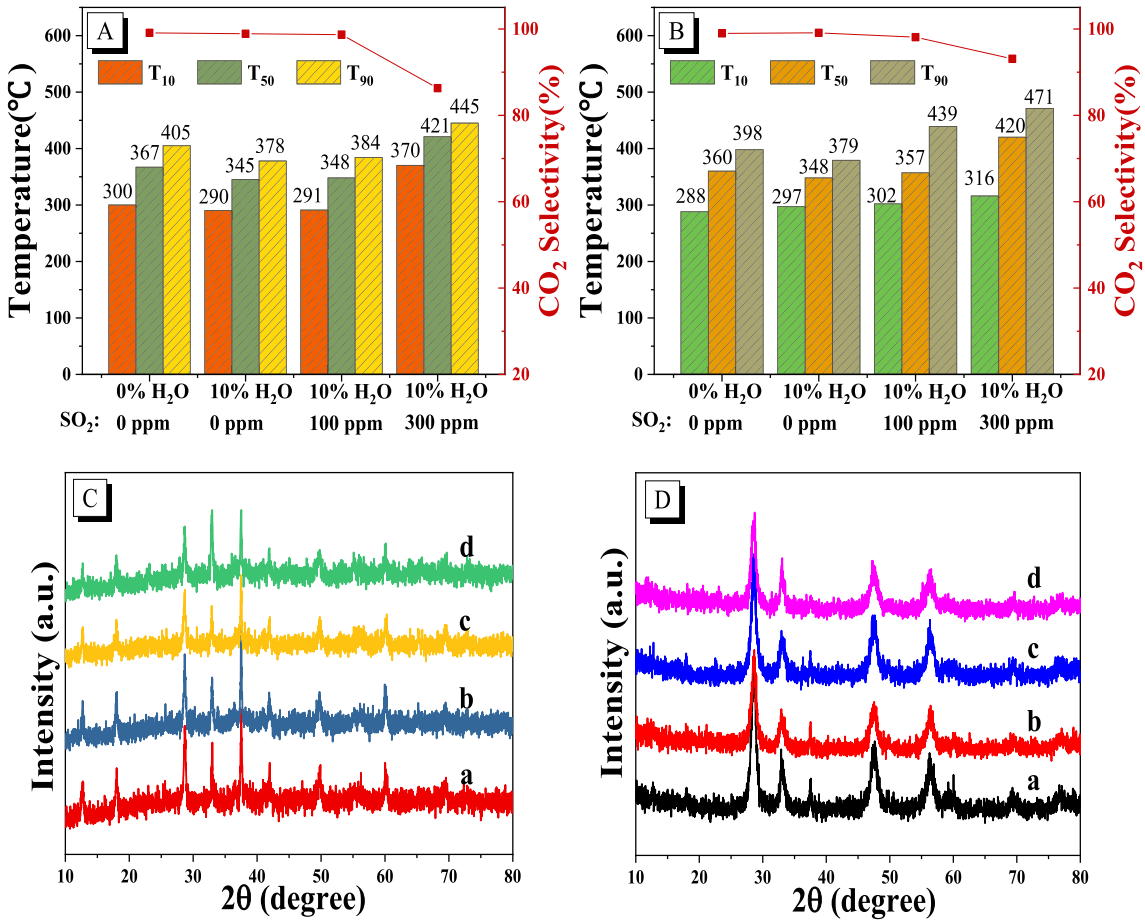



**Fig. 8.** The tolerance of sulfur dioxide and water of $MnO_x$ (A) and $Ce_1/MnO_x$ (B), X-ray diffraction patterns of used $MnO_x$ (C) and $Ce_1/MnO_x$ (D) under different treatment conditions (a: fresh catalyst; b: 10% $H_2O$ + 0 ppm$SO_2$; c: 10% $H_2O$ + 100 ppm$SO_2$; d: 10% $H_2O$ + 300 ppm$SO_2$).

which is further revealed the higher intrinsic activity of $Ce_1MnO_x$.

The adsorption and desorption rate of oxygen is great significant for the catalytic combustion of soot particles. At present, the direct characterization and detection for the adsorption and desorption rate of oxygen species on the catalyst are limited by the current characterization techniques. To investigate the rate of adsorption and desorption oxygen species, it is feasible to select soot particles as probe molecules to indirectly characterize the adsorption and desorption rates of oxygen species on the catalyst through the isothermal reaction [74]. The capacity of the adsorbed oxygen on the catalysts was verified by isothermal reaction under gaseous oxygen, while the capacity of the oxygen desorbed was obtained by anaerobic isothermal reaction. Fig. 10 shows the curves of $CO_2$ signal of $Ce_1MnO_x$ and $Ce_1/MnO_x$ catalysts obtained under aerobic and anaerobic isothermal reaction conditions at 250 °C. As depicted in Fig. 10, the curve of $CO_2$ signal shows the opposite trend under different conditions. There were remarkable changes of $CO_2$ signal within 300 s because of the instantaneous introduction and removal of gaseous oxygen. Moreover, the amorphous $Ce_1MnO_x$ was observed a striking variation in contrast to $Ce_1/MnO_x$, which further revealed that the amorphous catalyst possesses the ability to rapidly adsorb and release oxygen species. In addition, as shown in Table 7, $Ce_1MnO_x$ exhibited higher oxygen adsorption and desorption rate than $Ce_1/MnO_x$. When the reaction time was 300 s, the adsorption rate of $Ce_1MnO_x$ was $1.62 \times 10^{-7}$ mol·g$^{-1}$s$^{-1}$, which was 2.0 times as much as that of $Ce_1/MnO_x$, and the oxygen desorption rate was $0.92 \times 10^{-7}$ mol·g$^{-1}$s$^{-1}$, about 4.0 times that of $Ce_1/MnO_x$. Likewise, the adsorption rate of $Ce_1MnO_x$ ($1.88 \times 10^{-7}$ mol·g$^{-1}$s$^{-1}$) was about 2.9 times as much as that of $Ce_1/MnO_x$ ($0.65 \times 10^{-7}$ mol·g$^{-1}$s$^{-1}$), and the oxygen desorption rate was about 3.5 times that of $Ce_1/MnO_x$ when the reaction time was 3600 s. As expected, $Ce_1MnO_x$ has higher oxygen conversion efficiency than $Ce_1/MnO_x$, which plays an essential factor in accelerating the soot combustion.

The oxygen defect site plays a significant role during the soot oxidation reactions. Generally, it is practicable that the amount of oxygen defect sites is mainly related to the adsorption amount of surface active oxygens. Meanwhile, the soot-TPR can reflect the adsorption amount of surface active oxygens. Hence, the oxygen defect sites of $Ce_1MnO_x$ and $Ce_1/MnO_x$ catalysts were measured by soot-TPR [75,76]. Fig. 11 displays the soot-TPR curves(A) and peak fitting(B) of $Ce_1MnO_x$ and $Ce_1/MnO_x$ catalysts. According to $O_2$-TPD results of $Ce_1MnO_x$ and $Ce_1/MnO_x$ catalysts (Fig. 6Bc and 6Be), it can be seen from the Fig. 11A that the reduction peaks of three oxygen species appear at the range of 200 °C–500 °C, 500 °C–650 °C and 650 °C–750 °C, which are assigned to surface adsorbed oxygen, surface lattice oxygen and bulk lattice oxygen of the catalysts, respectively. As shown in Fig. 11B and Table 8, it was clearly demonstrated that the surface adsorbed oxygen content of $Ce_1MnO_x$ was ~ 42.92% and the adsorption amount of surface active oxygen ($O_{ad}$) was $6.81 \times 10^{-5}$ mol·g$^{-1}$. By comparison, the adsorption amount of surface active oxygen was $4.18 \times 10^{-5}$ mol·g$^{-1}$ for $Ce_1/MnO_x$. Obviously, the amount of surface adsorbed oxygen of $Ce_1MnO_x$ is about 1.62 times as much as that of $Ce_1/MnO_x$. The above significant difference between $Ce_1MnO_x$ and $Ce_1/MnO_x$ catalysts further proves that the amorphous catalyst has a stronger ability to adsorb oxygen species, that is, the $Ce_1MnO_x$ catalyst has a greater number of oxygen defect sites. On the other hand, Raman spectroscopy is an effective characterization for detecting oxygen defects. For further verification, the oxygen defect sites on the $Ce_1MnO_x$ and $Ce_1/MnO_x$ catalysts were further characterized by UV Raman. The UV Raman spectra of Fig. 12A shows that the band of

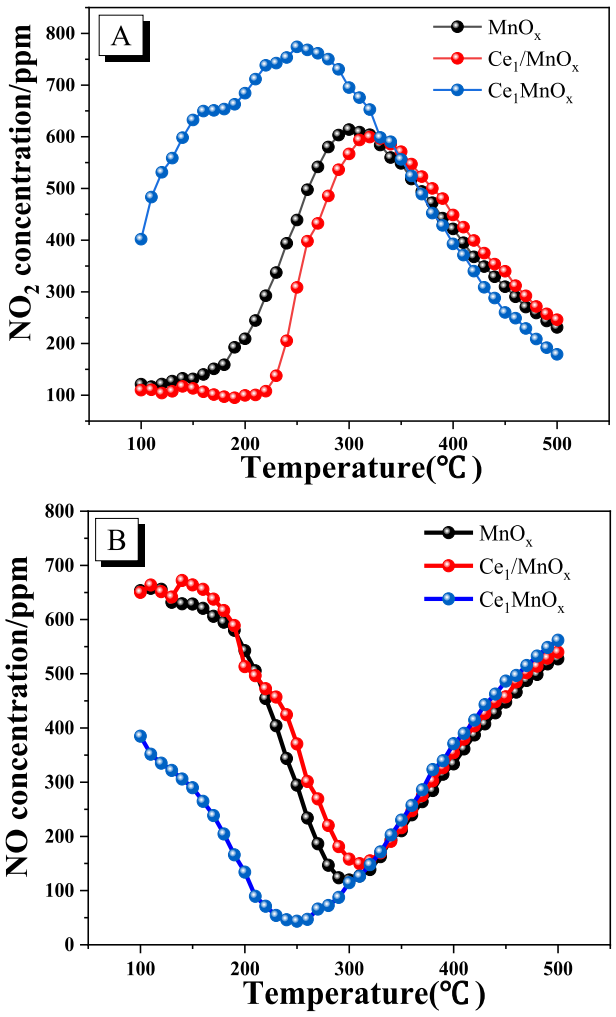



**Fig. 9.** $NO_2$ concentration (A) and NO concentration profiles (B) over $MnO_x$, $Ce_1/MnO_x$ and $Ce_1MnO_x$ catalysts.

**Table 6**
Reaction rate, active oxygen (O*) density and TOF values for soot combustion with $O_2$ over $Ce_1/MnO_x$ and $Ce_1MnO_x$ catalysts.

| Catalysts | Temperature/K[a] | V[b] (mols$^{-1}$g$^{-1}$ × 10$^{-7}$) | v*[c] (mols$^{-1}$m$^{-2}$ × 10$^{-9}$) | O*[d] (molg$^{-1}$ × 10$^{-4}$) | O* density[e] (nm$^{-2}$) | TOF[f] (s$^{-1}$ × 10$^{-3}$) |
|---|---|---|---|---|---|---|
| $Ce_1/MnO_x$ | 523 | 0.33 | 0.68 | 0.49 | 0.61 | 0.67 |
| $Ce_1MnO_x$ | 523 | 0.84 | 0.55 | 0.94 | 0.38 | 0.89 |

a: The K means the Kelvin temperature; b: Reaction rate; c: The specific reaction rate normalized by unit BET surface area; d: The number of active oxygen; e: The density of active oxygen; f: The ratio of the reaction rate to the active site density.

$Ce_1MnO_x$ and $Ce_1/MnO_x$ catalysts located at around 582 cm$^{-1}$, which was attributed to the oxygen defect sites (O-vacancies), and around 1171 cm$^{-1}$ to second-order longitudinal optical (2LO) mode [37,77]. In addition, the ratios of integral intensity ($A_{582}/A_{452}$) of catalysts can further reflect the relative O-vacancy concentration [78]. As shown in Fig. 12B, the ratios of integral intensity ($A_{582}/A_{452}$) of $Ce_1MnO_x$ is about 1.59 times that of $Ce_1/MnO_x$, indicating that the amorphous $Ce_1MnO_x$ possessed a higher amount of oxygen defect sites, which agrees well with the soot-TPR and TPO results.Fig. 12.U.Fig. 13.

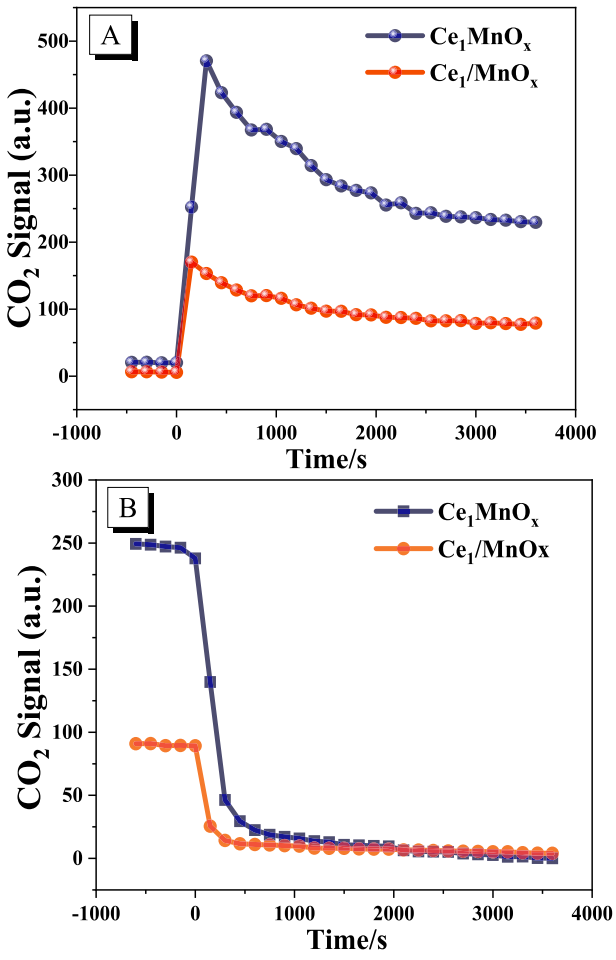



**Fig. 10.** $CO_2$ signal curves of $Ce_1MnO_x$ and $Ce_1/MnO_x$ catalysts under aerobic (A) and anaerobic (B) isothermal reaction conditions.

**Table 7**
Oxygen adsorption and desorption rate for soot combustion over $Ce_1/MnO_x$ and $Ce_1MnO_x$ catalysts.

| Catalysts | Temperature/K[a] | $v_1$[b] (mol·s$^{-1}$g$^{-1}$ × 10$^{-7}$) | $v_2$[c] (mol·s$^{-1}$g$^{-1}$ × 10$^{-7}$) | $v_3$[d] (mol·s$^{-1}$g$^{-1}$ × 10$^{-7}$) | $v_4$[e] (mol·s$^{-1}$g$^{-1}$ × 10$^{-7}$) |
|---|---|---|---|---|---|
| $Ce_1/MnO_x$ | 523 | 0.81 | 0.65 | 0.23 | 0.04 |
| $Ce_1MnO_x$ | 523 | 1.62 | 1.88 | 0.92 | 0.14 |

a: The K means the Kelvin temperature; b: Adsorption rate within 300 s; c: Adsorption rate within 3600 s; d: Desorption rate within 300 s; e: Desorption rate within 3600 s

Based on the above characterization and activity of the catalysts, the possible reaction mechanism over the $Ce_1/MnO_x$ and $Ce_1MnO_x$ catalysts could be proposed as follows. As shown in the Fig. 9, it is considered that there are two reaction pathways in the soot combustion process for the $Ce_1/MnO_x$ and $Ce_1MnO_x$ catalyst. The first reaction pathway is the direct oxidation of soot to be $CO_2$ by active oxygen species O*. The active species were formed by the adsorption and activation of gaseous oxygen by oxygen vacancies. Moreover, O* can be replenished continually by gaseous $O_2$ through oxygen vacancies. There are a handful of oxygen vacancies on the catalyst surface for $Ce_1/MnO_x$ catalyst because the synergistic effect between Ce and Mn for activation of $O_2$ is restricted by the excess $CeO_2$ on the surface of $MnO_x$. On the contrary, it can be inferred that the surface and interior of $Ce_1MnO_x$ catalyst has abundant

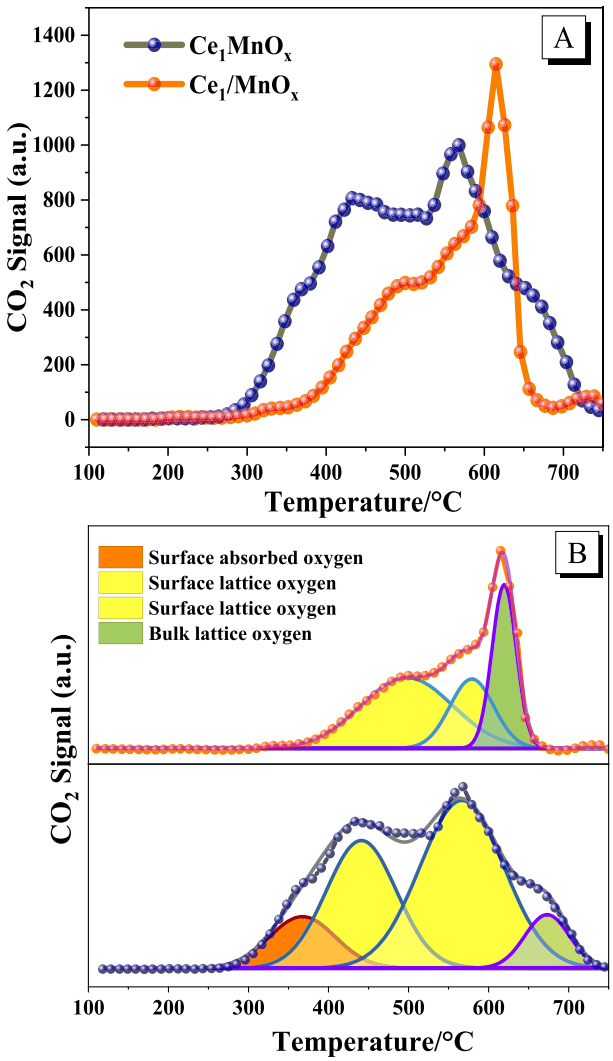



**Fig. 11.** soot-TPR curves (A) and peak fitting (B) of $Ce_1MnO_x$ and $Ce_1/MnO_x$ catalysts.

oxygen vacancies due to disordered lattice structures in the $Ce_1MnO_x$. The increased oxygen vacancy concentrations can accelerate the transition from gaseous oxygen to O*, which was verified by isothermal reaction under $O_2$. Thus, the active oxygen species formation and release rate of $Ce_1MnO_x$ catalyst are essential for attaining high activity. The second reaction pathway is the oxidation of soot by $NO_2$ converted from NO, which is formed indirectly by the oxidation of O*. The $NO_2$ produced by NO oxidation provides more powerful oxidation for soot combustion. Furthermore, $NO_2$ may be stay in the oxygen vacancies to improve the $NO_x$ storage capacity of catalyst. In this pathway, $Ce_1MnO_x$ also has faster reaction rate than that of $Ce_1/MnO_x$, that is, $Ce_1MnO_x$ has excellent NO oxidation ability in contrast to $Ce_1/MnO_x$, which is proved by NO-TPO tests. Hence, the abundant oxygen vacancies and better catalytic ability for NO oxidation endowed the amorphous $Ce_1MnO_x$ catalyst with outstanding soot oxidation activity.

## 4. Conclusion

A series of amorphous cerium–manganese oxide catalysts were successfully synthetized via a simple hydrothermal process. The effects of Ce doping amounts and calcination temperature on the physicochemical characteristics of cerium–manganese oxide catalysts were investigated. The amorphous $Ce_nMnO_x$ catalysts exhibited excellent activity for soot oxidation. Doping with Ce dramatically accelerate soot combustion process, and the resulting catalysts showed high $CO_2$ selectivity and good stability. Among the prepared catalysts, $Ce_1MnO_x$ calcinated at 450 °C had the best catalytic activity, the values of $T_{10}$, $T_{50}$ and $T_{90}$ were 258 °C, 327 °C and 370 °C, respectively. The characterization such as XRD, SEM, $N_2$ physisorption, $H_2$-TPR and $O_2$-TPD confirmed that the amorphous $Ce_1MnO_x$ catalyst presented high oxygen mobility and high adsorption capacity for oxygen species. Meanwhile, Ce doping significantly affected the texture properties of the catalyst. The Ce-induced enhancements in specific surface area and accumulated pores of

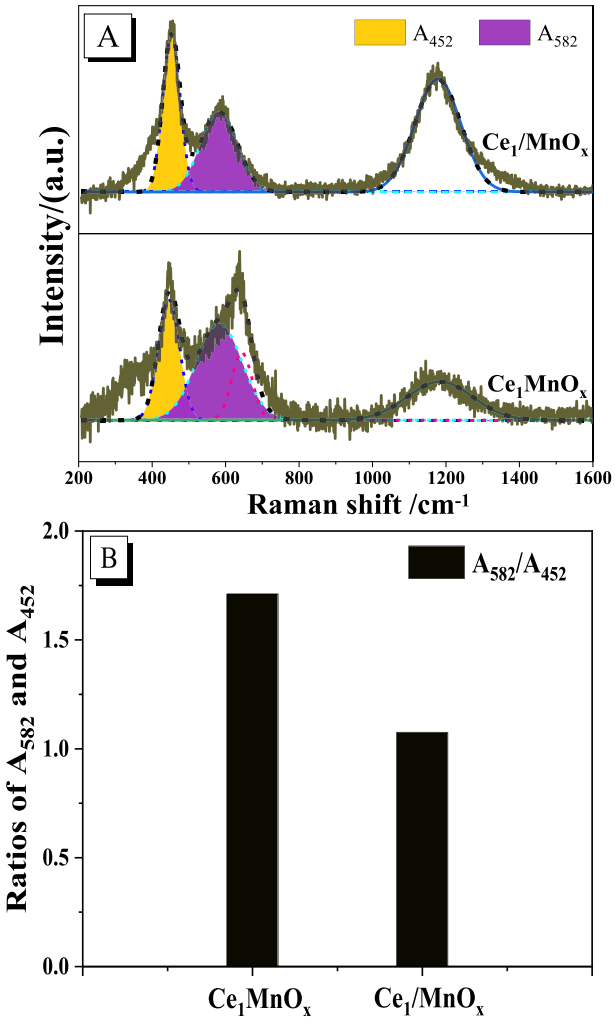



**Fig. 12.** UV Raman spectra (A) and the concentration of surface oxygen vacancies (B) of $Ce_1MnO_x$ and $Ce_1/MnO_x$ catalysts.

**Table 8**
Peak temperatures of soot-TPR and the adsorption amount of surface active oxygen over $Ce_1/MnO_x$ and $Ce_1MnO_x$ catalysts.

| Catalysts | Peak I | | Peak II | | Peak III | | Peak IV | | $O_{ad}$ molg$^{-1}$ × $10^{-5}$) |
|---|---|---|---|---|---|---|---|---|---|
| | T/ °C | R/% | T/ °C | R/% | T/°C | R/% | T/ °C | R/% | |
| $Ce_1/MnO_x$ | 331 | 0.21 | 497 | 47.87 | 579 | 22.56 | 619 | 29.36 | 4.18 |
| $Ce_1MnO_x$ | 367 | 11.82 | 440 | 31.10 | 566 | 48.81 | 673 | 8.27 | 6.81 |

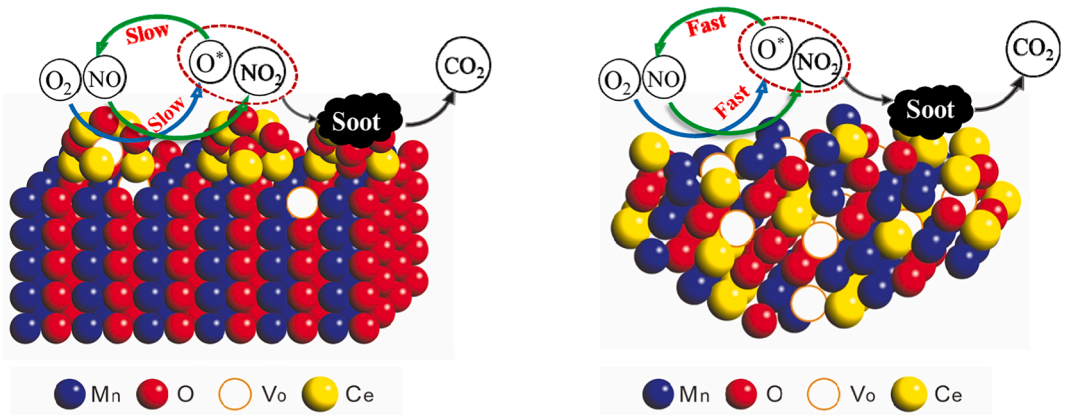



**Fig. 13.** The possible reaction mechanism for soot combustion on $Ce_1/MnO_x$ and $Ce_1MnO_x$ catalysts.

$Ce_1MnO_x$ catalyst improved the effective contact between the catalyst and soot, while also facilitating the diffusion and activation of micro-molecular gases. The amorphous $Ce_nMnO_x$ catalyst, which exhibits the advantages of low cost, simple synthesis, high catalytic performance and good stability, has potential application prospect in diesel soot combustion.

## CRediT authorship contribution statement

**Di Yu:** Data curation, Formal analysis, Investigation, Methodology, Writing - original draft. **Chao Peng:** Data curation, Formal analysis, Investigation, Methodology, Writing - original draft. **Xuehua Yu:** Data curation, Formal analysis, Investigation, Methodology, Writing - original draft. **Lanyi Wang:** Data curation, Formal analysis, Visualization. **Kaixiang Li:** Data curation, Formal analysis, Investigation. **Zhen Zhao:** Conceptualization, Funding acquisition, Project administration, Resources, Supervision, Validation, Writing - review & editing. **Zhenguo Li:** Conceptualization, Formal analysis, Investigation.

## Declaration of Competing Interest

The authors declare that they have no known competing financial interests or personal relationships that could have appeared to influence the work reported in this paper.

## Acknowledgements

This work was supported by NSFC (22072095, U1908204, 21761162016); Key Research and Development Program of MOST (2017YFE0131200) for collaboration between China and Poland; General Projects of Liaoning Province Natural Fund (2019-MS-284); National Engineering Laboratory for Mobile Source Emission Control Technology (NELMS2018A04); University level innovation team of Shenyang Normal University; Major Incubation Program of Shenyang Normal University (ZD201901).

## References

[1] Frank B, Schuster ME, Schlögl R, Su DS. Emission of highly activated soot particulate — The other side of the coin with modern diesel engines. Angew Chem Int Ed 2013;52:2673–7.
[2] Fino D, Bensaid S, Piumetti M, Russo N. A review on the catalytic combustion of soot in Diesel particulate filters for automotive applications: from powder catalysts to structured reactors. Appl Catal A: Gen 2016;509:75–96.
[3] Gentner DR, Jathar SH, Gordon TD, Bahreini R, Day DA, El Haddad I, et al. Review of urban secondary organic aerosol formation from gasoline and diesel motor vehicle emissions. Environ Sci Technol 2017;51:1074–93.
[4] Zhu H, Bohac SV, Nakashima K, Hagen LM, Huang Z, Assanis DN. Effect of fuel oxygen on the trade-offs between soot, $NO_x$ and combustion efficiency in premixed low-temperature diesel engine combustion. Fuel 2013;112:459–65.
[5] Dhal GC, Mohan D, Prasad R. Preparation and application of effective different catalysts for simultaneous control of diesel soot and $NO_x$ emissions: an overview. Catal Sci Technol 2017;7:1803–25.
[6] Lizarraga L, Souentie S, Boreave A, George C, D'Anna B, Vernoux P. Effect of diesel oxidation catalysts on the diesel particulate filter regeneration process. Environ Sci Technol 2011;45:10591–7.
[7] Di Sarli V, Di Benedetto A. Combined effects of soot load and catalyst activity on the regeneration dynamics of catalytic diesel particulate filters. AIChE J 2018;64:1714–22.
[8] Wei Y, Liu J, Zhao Z, Chen Y, Xu C, Duan A, et al. Highly active catalysts of gold nanoparticles supported on three-dimensionally ordered macroporous $LaFeO_3$ for soot oxidation. Angew Chem Int Ed 2011;50:2326–9.
[9] Serve A, Boreave A, Cartoixa B, Pajot K, Vernoux P. Synergy between Ag nanoparticles and yttria-stabilized zirconia for soot oxidation. Appl Catal B: Environ 2019;242:140–9.
[10] Corro G, Flores A, Pacheco-Aguirre F, Pal U, Bañuelos F, Ramirez A, et al. Biodiesel and fossil-fuel diesel soot oxidation activities of $Ag/CeO_2$ catalyst. Fuel 2019;250:17–26.
[11] Yu X, Wang L, Chen M, Fan X, Zhao Z, Cheng K, et al. Enhanced activity and sulfur resistance for soot combustion on three-dimensionally ordered macroporous-mesoporous $Mn_xCe_{1-x}O_\delta/SiO_2$ catalysts. Appl Catal B: Environ 2019;254:246–59.
[12] Yu XH, Zhao Z, Wei YC, Liu J. Ordered micro/macro porous K-OMS-2/$SiO_2$ nanocatalysts: facile synthesis, low cost and high catalytic activity for diesel soot combustion. Sci Rep 2017;7:43894.
[13] Zhai G, Wang J, Chen Z, Yang S, Men Y. Highly enhanced soot oxidation activity over 3DOM $Co_3O_4$-$CeO_2$ catalysts by synergistic promoting effect. J Hazard Mater 2019;363:214–26.
[14] Lee C, Park J-I, Shul Y-G, Einaga H, Teraoka Y. Ag supported on electrospun macro-structure $CeO_2$ fibrous mats for diesel soot oxidation. Appl Catal B: Environ 2015;174-175:185–92.
[15] Alcalde-Santiago V, Davó-Quiñonero A, Lozano-Castelló D, Bueno-López A. On the soot combustion mechanism using 3DOM ceria catalysts. Appl Catal B: Environ 2018;234:187–97.
[16] He JS, Yao P, Qiu J, Zhang HL, Jiao Y, Wang JL, et al. Enhancement effect of oxygen mobility over Ce0.5Zr0.5O2 catalysts doped by multivalent metal oxides for soot combustion. Fuel 2021;286:119359.
[17] Si W, Wang Yu, Peng Y, Li J. Selective dissolution of A-site cations in $ABO_3$ perovskites: a new path to high-performance catalysts. Angew Chem Int Ed 2015;127:8065–8.
[18] Fang F, Feng N, Wang L, Meng J, Liu G, Zhao P, et al. Fabrication of perovskite-type macro/mesoporous $La_{1-x}K_xFeO_{3-\delta}$ nanotubes as an efficient catalyst for soot combustion. Appl Catal B: Environ 2018;236:184–94.
[19] Zou G, Chen M, Shangguan W. Promotion effects of $LaCoO_3$ formation on the catalytic performance of Co-La oxides for soot combustion in air. Catal Commun 2014;51:68–71.
[20] Li Z, Meng M, Dai F, Hu T, Xie Y, Zhang J. Performance of K and Ni substituted $La_{1-x}K_xCo_{1-y}Ni_yO_{3-\delta}$ perovskite catalysts used for soot combustion, NOx storage and simultaneous NOx-soot removal. Fuel 2012;93:606–10.
[21] Cheng Li, Men Y, Wang J, Wang H, An W, Wang Y, et al. Crystal facet-dependent reactivity of α-$Mn_2O_3$ microcrystalline catalyst for soot combustion. Appl Catal B: Environ 2017;204:374–84.
[22] Xu H, Yan N, Qu Z, Liu W, Mei J, Huang W, et al. Gaseous heterogeneous catalytic reactions over Mn-based oxides for environmental applications: a critical review. Environ Sci Technol 2017;51:8879–92.
[23] Cao J, Wu F, Wen M, Peng J, Yang Y, Dong H. Adsorption mechanism of typical VOCs on pristine and Al-modified $MnO_2$ monolayer. Appl Surf Sci 2021;539:48164.
[24] Zeng X, Li Bo, Liu R, Li X, Zhu T. Investigation of promotion effect of Cu doped $MnO_2$ catalysts on ketone-type VOCs degradation in a one-stage plasma-catalysis system. Chem Eng J 2020;384:123362.
[25] Wang P, Duan J, Wang J, Mei F, Liu P. Elucidating structure-performance correlations in gas-phase selective ethanol oxidation and CO oxidation over metal-doped γ-$MnO_2$. Chin J Catal 2020;41:1298–310.

[26] Wei Lu, Cui S, Guo H. Study the low-temperature SCR property of M-doped (M=Ni, Cr Co, Se, Sn) MnO2(100) through density functional theory (DFT): Improvement of sulfur poisoning resistance. Mol Catal 2018;459:31–7.
[27] Jampaiah D, Velisoju VK, Venkataswamy P, Coyle VE, Nafady A, Reddy BM, et al. Nanowire morphology of mono- and bidoped α-$MnO_2$ catalysts for remarkable enhancement in soot oxidation. ACS Appl Mater Interfaces 2017;9:32652–66.
[28] Zhang H, Yuan S, Wang JianLi, Gong MaoChu, Chen Y. Effects of contact model and $NO_x$ on soot oxidation activity over Pt/$MnO_x$-$CeO_2$ and the reaction mechanisms. Chem Eng J 2017;327:1066–76.
[29] Lavande NR, More RK, More PM. Mg modified $MnO_x$-$CeO_{2-\delta}$ catalyst for low temperature complete oxidation of simulated diesel engine exhaust. Appl Surf Sci 2020;502:144299.
[30] Mukherjee D, Venkataswamy P, Devaiah D, Rangaswamy A, Reddy BM. Crucial role of titanium dioxide support in soot oxidation catalysis of manganese doped ceria. Catal Sci Technol 2017;7:3045–55.
[31] Kuwahara Y, Fujibayashi A, Uehara H, Mori K, Yamashita H. Catalytic combustion of diesel soot over Fe and Ag-doped manganese oxides: role of heteroatoms in the catalytic performances. Catal Sci Technol 2018;8:1905–14.
[32] Kwon HJ, Hyun Baik J, Tak Kwon Y, Nam I-S, Oh SH. Detailed reaction kinetics over commercial three-way catalysts. Chem Eng Sci 2007;62:5042–7.
[33] Kusatsugu K, Nakamura Y, Haneda M. Three-way catalytic performance of Fe-doped Pd/$CeO_2$-$ZrO_2$ under lean/rich perturbation conditions. Appl Catal A: Gen 2019;587:117268.
[34] Machida M, Ueno M, Omura T, Kurusu S, Hinokuma S, Nanba T, et al. $CeO_2$-grafted Mn-Fe oxide composites as alternative oxygen-storage materials for three-way catalysts: laboratory and chassis dynamometer tests. Ind Eng Chem Res 2017;56:3184–93.
[35] Ozawa M, Misaki M, Iwakawa M, Hattori M, Kobayashi K, Higuchi K, et al. Low content Pt-doped $CeO_2$ and core-shell type $CeO_2$/$ZrO_2$ model catalysts; microstructure, TPR and three way catalytic activities. Catal Today 2019;332:251–8.
[36] Ma J, Wang C, He H. Transition metal doped cryptomelane-type manganese oxide catalysts for ozone decomposition. Appl Catal B: Environ 2017;201:503–10.
[37] Sun M, Yu L, Ye F, Diao G, Yu Q, Hao Z, et al. Transition metal doped cryptomelane-type manganese oxide for low-temperature catalytic combustion of dimethyl ether. Chem Eng J 2013;220:320–7.
[38] Lin X, Li S, He H, Wu Z, Wu J, Chen L, et al. Evolution of oxygen vacancies in $MnO_x$-$CeO_2$ mixed oxides for soot oxidation. Appl Catal B: Environ 2018;223:91–102.
[39] He H, Lin X, Li S, Wu Z, Gao J, Wu J, et al. The key surface species and oxygen vacancies in $MnO_x$(0.4)-$CeO_2$ toward repeated soot oxidation. Appl Catal B: Environ 2018;223:134–42.
[40] Zhang H, Zhou C, Galvez ME, Da Costa P, Chen Y. $MnO_x$-$CeO_2$ mixed oxides as the catalyst for NO-assisted soot oxidation: the key role of NO adsorption/desorption on catalytic activity. Appl Surf Sci 2018;462:678–84.
[41] Ravi S, Winfred Shashikanth F. Preparation of Mn doped $CeO_2$ nanoparticles with enhanced ferromagnetism. Mater Chem Phys Mater Chem Phys 2017;194:37–41.
[42] Kumar P, Kumar P, Kumar A, Meena RC, Tomar R, Chand F, et al. Structural, morphological, electrical and dielectric properties of Mn doped $CeO_2$. J Alloys Compd 2016;672:543–8.
[43] Chong S, Wu Y, Liu C, Chen Y, Guo S, Liu Y, et al. Cryptomelane-type $MnO_2$/carbon nanotube hybrids as bifunctional electrode material for high capacity potassium-ion full batteries. Nano Energy 2018;54:106–15.
[44] Hou J, Liu L, Li Y, Mao M, Lv H, Zhao X. Tuning the $K^+$ concentration in the tunnel of OMS-2 nanorods leads to a significant enhancement of the catalytic activity for benzene oxidation. Environ Sci Technol 2013;47:13730–6.
[45] Sheng Y, Zhou Y, Lu H, Zhang Z, Chen Y. Soot combustion performance and $H_2$-TPR study on ceria-based mixed oxides. Chin J of Catal 2013;34:567–77.
[46] Tang W, Wu X, Li D, Wang Z, Liu G, Liu H, et al. Oxalate route for promoting activity of manganese oxide catalysts in total VOCs' oxidation: effect of calcination temperature and preparation method. J Mater Chem A 2014;2:2544–54.
[47] Wang R, Li J. Effects of precursor and sulfation on OMS-2 catalyst for oxidation of ethanol and acetaldehyde at low temperatures. Environ Sci Technol 2010;44:4282–7.
[48] King'ondu CK, Opembe N, Chen C-h, Ngala K, Huang H, Iyer A, et al. Manganese oxide octahedral molecular sieves (OMS-2) multiple framework substitutions: a new route to OMS-2 particle size and morphology control. Adv Funct Mater 2011;21:312–23.
[49] Luo Y, Deng Y-Q, Mao W, Yang X-J, Zhu K, Xu J, et al. Probing the surface structure of α-$Mn_2O_3$ Nanocrystals during CO oxidation by operando Raman Spectroscopy. J Phys Chem C 2012;116:20975–81.
[50] Xing L, Yang Y, Cao C, Zhao D, Gao Z, Ren W, et al. Decorating $CeO_2$ nanoparticles on $Mn_2O_3$ nanosheets to improve catalytic soot combustion. ACS Sustainable Chem Eng 2018;6:16544–54.
[51] Hou J, Li Y, Liu L, Ren Lu, Zhao X. Effect of giant oxygen vacancy defects on the catalytic oxidation of OMS-2 nanorods. J Mater Chem A 2013;1:6736–41.
[52] Wang C, Ma J, Liu F, He H, Zhang R. The Effects of $Mn^{2+}$ Precursors on the Structure and Ozone Decomposition Activity of Cryptomelane-Type Manganese Oxide (OMS-2) Catalysts. J Phys Chem C 2015;119(40):23119–26.
[53] Lee Y, He G, Akey AJ, Si R, Flytzani-Stephanopoulos M, Herman IP. Raman Analysis of Mode Softening in Nanoparticle $CeO_{2-\delta}$ and Au-$CeO_{2-\delta}$ during CO Oxidation. J Am Chem Soc 2011;133(33):12952–5.
[54] Spanier JE, Robinson RD, Zhang F, Chan SW, Herman IP. Size-dependent properties of $CeO_{2-y}$ nanoparticles as studied by Raman scattering. Phys Rev B 2001;64:245407.
[55] Li Y, Sun Q, Kong M, Shi W, Huang J, Tang J, et al. Coupling oxygen ion conduction to photocatalysis in mesoporous nanorod-like ceria significantly improves photocatalytic efficiency. J Phys Chem C 2011;115:14050–7.
[56] Zhang Y, Zhang L, Deng J, Dai H, He H. Controlled Synthesis, Characterization, and Morphology-Dependent Reducibility of Ceria-Zirconia-Yttria Solid Solutions with Nanorod-like, Microspherical, Microbowknot-like, and Micro-octahedral Shapes. Inorg Chem 2009;48:2181–92.
[57] Niu F, Zhang D, Shi L, He X, Li H, Mai H, et al. Facile synthesis, characterization and low-temperature catalytic performance of Au/$CeO_2$ nanorods. Mater Lett 2009;63:2132–5.
[58] Galakhov VR, Demeter M, Bartkowski S, Neumann M, Ovechkina NA, Kurmaev EZ, et al. Mn 3s exchange splitting in mixed-valence manganites. Phys Rev B 2002;65:1131021–4.
[59] Chen Z, Yang Q, Li H, Li X, Wang L, Chi Tsang S. Cr-$MnO_x$ mixed-oxide catalysts for selective catalytic reduction of $NO_x$ with $NH_3$ at low temperature. J Catal 2010;276:56–65.
[60] Venezia AM, Di Carlo G, Pantaleo G, Liotta LF, Melaet G, Kruse N. Oxidation of $CH_4$ over Pd supported on $TiO_2$-doped $SiO_2$: effect of Ti(IV) loading and influence of $SO_2$. Appl Catal B: Environ 2009;88:430–7.
[61] Biesinger MC, Payne BP, Grosvenor AP, Lau LWM, Gerson AR, Smart RSC. Resolving surface chemical states in XPS analysis of first row transition metals, oxides and hydroxides: Cr, Mn, Fe. Co and Ni. Appl Surf Sci 2011;257(7):2717–30.
[62] Chen H, Sayari A, Adnot A, Larachi Faiçal. Composition–activity effects of Mn-Ce-O composites on phenol catalytic wet oxidation. Appl Catal B: Environ 2001;32:195–204.
[63] Vaz CAF, Wang H-Q, Ahn CH, Henrich VE, Baykara MZ, Schwendemann TC, et al. Interface and electronic characterization of thin epitaxial films. Surf Sci 2009;603:291–7.
[64] Natile MM, Glisenti A. $CoO_x$/$CeO_2$ nanocomposite powders: synthesis, characterization, and reactivity. Chem Mater 2005;17:3403–14.
[65] Ding Y-S, Shen X-F, Sithambaram S, Gomez S, Kumar R, Crisostomo VMB, et al. Synthesis and catalytic activity of cryptomelane-type manganese dioxide nanomaterials produced by a novel solvent-free method. Chem Mater 2005;17:5382–9.
[66] Santos VP, Pereira MFR, Órfão JJM, Figueiredo JL. The role of lattice oxygen on the activity of manganese oxides towards the oxidation of volatile organic compounds. Appl Catal B: Environ 2010;99:353–63.
[67] Makwana V. The role of lattice oxygen in selective benzyl alcohol oxidation using OMS-2 catalyst: a kinetic and isotope-labeling study. J Catal 2002;210:46–52.
[68] Chen D, He D, Lu J, Zhong L, Liu F, Liu J, et al. Investigation of the role of surface lattice oxygen and bulk lattice oxygen migration of cerium-based oxygen carriers: XPS and designed $H_2$-TPR characterization. Appl Catal B: Environ 2017;218:249–59.
[69] Liu Y, Zhou H, Cao R, Sun T, Zong W, Zhan J, et al. Different behaviors of birnessite-type $MnO_2$ modified by Ce and Mo for removing carcinogenic airborne benzene. Mater Chem Phys 2019;221:457–66.
[70] Zhang L, Tu J, Lyu L, Hu C. Enhanced catalytic degradation of ciprofloxacin over Ce-doped OMS-2 microspheres. Appl Catal B: Environ 2016;181:561–9.
[71] Yin Y-G, Xu W-Q, DeGuzman R, Suib SL, O'Young CL. Studies of stability and reactivity of synthetic cryptomelane-like manganese oxide octahedral molecular sieves. Inorg Chem 1994;33:4384–9.
[72] Kaliaguine S, Van Neste A, Szabo V, Gallot JE, Bassir M, Muzychuk R. Perovskite-type oxides synthesized by reactive grinding: part I. Preparation and characterization. Appl Catal A: Gen 2001;209(1-2):345–58.
[73] Levasseur B, Kaliaguine S. Effects of iron and cerium in $La_{1-y}Ce_yCo_{1-x}Fe_xO_3$ perovskites as catalysts for VOC oxidation. Appl Catal B: Environ 2009;88:305–14.
[74] Zhang Z, Han D, Wei S, Zhang Y. Determination of active site densities and mechanisms for soot combustionwith $O_2$ on Fe-doped $CeO_2$ mixed oxides. J Catal 2010;276:16–23.
[75] Cao C, Xing L, Yang Y, Tian Ye, Ding T, Zhang J, et al. Dieselsoot elimination over potassium-promoted $Co_3O_4$ nanowires monolithic catalysts under gravitation contact mode. Appl Catal B: Environ 2017;218:32–45.
[76] Yang Y, Zhao D, Gao Z, Tian Ye, Ding T, Zhang J, et al. Interface interaction induced oxygen activation of cactus-like $Co_3O_4$/OMS-2 nanorod catalysts in situ grown on monolithic cordierite for diesel soot combustion. Appl Catal B: Environ 2021;286:119932.
[77] Taniguchi T, Watanabe T, Sugiyama N, Subramani AK, Wagata H, Matsushita N, et al. Identifying defects in ceria-based nanocrystals by UV resonance Raman Spectroscopy. J Phys Chem C 2009;113(46):19789–93.
[78] Wu Z, Li M, Howe J, Meyer HM, Overbury SH. Probing defect sites on $CeO_2$ nanocrystals with well-defined surface planes by Raman Spectroscopy and $O_2$ adsorption. Langmuir 2010;26:16595–606.